Singularity Resolution and Dynamical Black Holes

In fulfillment of the master of science degree in theoretical physics.

Jonathan Ziprick

Department of Physics and Astronomy

University of Manitoba

Winnipeg, Manitoba, Canada

This thesis was defended on April 3 and submitted

to the Faculty of Graduate Studies on April 8, 2009.

Abstract

We study the effects of loop quantum gravity (LQG) motivated corrections in classical systems. Computational methods are used to simulate black hole formation from the gravitational collapse of a massless scalar field in Painlevé-Gullstrand (PG) coordinates. Singularities present in the classical case are resolved by a radiation-like phase in the quantum collapse. The evaporation is not complete but leaves behind an outward moving shell of mass that disperses to infinity. We reproduce Choptuik scaling showing the usual behaviour for the curvature scaling, while observing previously unseen behaviour in the mass scaling. The quantum corrections are found to impose a lower limit on black hole mass and generate a new universal power law scaling relationship. In a parallel study, we quantize the Hamiltonian for a particle in the singular $1/r^2$ potential, a form that appears frequently in black hole physics. In addition to conventional Schrödinger methods, the quantization is performed using full and semiclassical polymerization. The various quantization schemes are in excellent agreement for the highly excited states but differ for the low-lying states, and the polymer spectrum is bounded below even when the Schrödinger spectrum is not.

Dedication

This work is dedicated to my loving wife Anastasia who encouraged me to return to school to study physics when I was toiling away as a mechanical engineer. I would not have been brave enough to follow this path without your support. Thank you for standing by me through the many hours of hard work in all these years of schooling. Any success I have as a physicist is owed to you.

Acknowledgments

First and foremost, the work herein is a credit to my advisor, Gabor Kunstatter. I am proud of this thesis, and know that I could not have done research at this level with anyone else. Gabor knows a great deal about physics and is able to pass this on to others. He treats everyone with respect and understands the motivating value of compliments, while being able to point out shortcomings without discouragement. He is a person of rare quality, possessing knowledge of a wide array of subjects while remaining modest and being well-liked by everyone. When faced with a difficult situation, I have only to ask myself "What would Gabor do?", and the way becomes clear.

Through Gabor, I had the good fortune to meet and work with Jorma Louko at the University of Nottingham. Jorma has an exceptional knowledge of mathematical physics and is able to present complicated ideas in a clear and understandable manner. Beyond this, he is kind, helpful and considerate. It has been an honour to collaborate with a researcher of his calibre.

I thank Thomas Osborn and William Kocay for being members of my thesis examining committee. It was a challenge to prepare for the difficult questions that I anticipated at the defence. It was comforting to know these questions would be presented in a respectful and non-confrontational manner. I have been privileged to learn from the rigorous teaching of Dr. Osborn, one of the finest professors I have come across in all of my university experience. Dr.

Kocay was the external examiner. He made a very good impression on me in our one meeting prior to the defence, and helped to speed up the computer code which proved invaluable for working with numerical resolutions that were fine enough to produce good results.

I commend the physics departments at both the University of Manitoba and the University of Winnipeg for working in cooperation to allow for students like me with connections to both schools. I have spent much of my time at the Univesity of Winnipeg over the last few years and have gotten to know many of the faculty in this time. A few of you stand out for teaching many of my courses and frequently speaking with me outside of class to provide help with course work and advice in career decisions: Dwight Vincent, Jeff Martin, Randy Kobes — thank you.

There are many people who have provided helpful discussions and correspondence that was integral to this research. In this regard I thank Alex Buchel, Ramin Daghigh, David Garfinkle, Jack Gegenberg, Sven Gnutzmann, Carsten Gundlach, Viqar Husain, Kayll Lake, Hideki Maeda, Robert Mann and Ari Peltola.

I thank Westgrid for providing computer resources that were used to run many of the simulations. And finally, I am grateful for the funding given by the Natural Sciences and Engineering Research Council of Canada that made all of this work possible.

Contents

Abstract **i**

Dedication **ii**

Acknowledgments **iii**

Publications **ix**

Prologue **xi**

1 $1/r^2$ Potential **1**

1.1 Introduction 1

1.2 Schrödinger Quantization 4

1.2.1 $\lambda > 1/4$ 6

1.2.2 $\lambda = 1/4$ 10

1.2.3 $-3/4 < \lambda < 1/4$ 10

1.2.4 $\lambda \leq -3/4$ 11

1.3 Polymer Quantization 12

1.3.1 Semiclassical Polymer Theory 13

1.3.2 Full Quantum Polymer Theory 17

1.3.3 Eigenstates and the Numerical Method 20
1.4 Results 22
1.5 Conclusions 26

2 Dynamical Black Holes **29**
2.1 Introduction 29
2.2 Critical Behaviour 32
2.3 Equations of Motion 36
2.4 Computational Methods 45
2.5 Quantum Corrections 49
2.6 Results 52
2.6.1 Classical Black Holes 52
2.6.2 Quantum Black Holes 58
2.7 Conclusion 64

Epilogue **66**

List of Tables

1.1 The lowest five eigenvalues of the regulated potential 23

1.2 Lowest five eigenvalues of the unregulated Coulomb potential 28

2.1 The critical exponent and period of the mass scaling curve for various initial data and mesh resolutions 55

List of Figures

1.1 Regulated and unregulated forms of the $-1/x^2$ potential 21

1.2 The lowest two energy levels as a function of λ 24

1.3 $\ln(-\mu^2 E_n)$ vs. n 25

1.4 β vs. α 26

2.1 Spacetime diagram of black hole formation 31

2.2 Phase space diagram of the collapse solutions 34

2.3 $f_{unreg}(r)$, $f_{reg}(r)$ and f_{smooth}(r) 51

2.4 Classical black hole spacetimes 52

2.5 $\psi(r=0)$ vs. τ 54

2.6 Classical curvature scaling 57

2.7 Classical mass scaling, $\Delta r(r=0)/r_0 = 10^{-4}$ 58

2.8 Classical mass scaling, $\Delta r(r=0)/r_0 = 10^{-5}$ 59

2.9 Quantum black hole spacetimes 60

2.10 Quantum mass scaling 62

2.11 p_{q*} vs. μ 63

Publications

Three articles were produced from this work so far:

a. G. Kunstatter, J. Louko and J. Ziprick, "Polymer quantization, singularity resolution and the $1/r^2$ potential", Phys. Rev. A 79, 032104 (2009), arXiv:0812.0993v1 [gr-qc].

b. J. Ziprick and G. Kunstatter, "Spherically Symmetric Black Hole Formation in Painlevé-Gullstrand Coordinates", arXiv:0812.0993v1 [gr-qc] (Dec. 2008).

c. J. Ziprick and G. Kunstatter, "Dynamical Singularity Resolution in Spherically Symmetric Black Hole Formation", arXiv:0902.3224v1 [gr-qc] (Feb. 2009).

[a] has been published in Physical Review A. My work on this project was to perform the full polymer quantization of the $1/r^2$ potential using analytical and numerical methods, study the system using the code I had written and author the corresponding sections of the article.

A shortened version of [b] has been submitted to Physical Review D Rapid Communications and is currently with referees. [c] has been submitted to Physical Review Letters. Under the guidance of my advisor (GK), I undertook the bulk of the research for these papers and was the first author on both, although GK contributed a great deal to the writing through valuable additions and improvements.

These articles constitute a large portion of this document. Some definitions of techinical terms were added, and small changes were made to wording and notation where required to improve the overall flow of the thesis. The first chapter is based on [a] with added detail in the mathematics that were not present in the article. The second chapter involves the study of dynamical black holes in both classical and quantum settings. [b] is a study of the classical system only. Chapter 2 uses relevant portions of [b] with added detail to the calculations and numerical methods, and introduces a large amount of new material on the quantum theory. [c] was written after the first draft of this thesis. [b] and [c] are both short letters. A fourth article which presents a rigorous derivation of our methods and a larger analysis of results will soon be written.

Prologue

General relativity and quantum mechanics stand out as the two great achievements of modern theoretical physics. Over the last century many great minds have pursued the unification of these ideas into a single theory of quantum gravity, but a satisfactory solution has yet to be found. Gravity remains the only fundamental force in nature lacking a consistent quantum description.

One of the main hindrances in developing a quantum theory of gravity has been the complete lack of experimental evidence to guide research and test ideas. Fortunately, the phenomenology of quantum gravity is beginning to generate a great deal of interest, with several exciting prospects lying on the distant horizon of experimental research [1]. Until these ideas can be implemented, progress must continue to come by way of theory, with mathematical models to serve as the testing grounds.

Two of the leading approaches to quantum gravity are string theory and loop quantum gravity (LQG). LQG is a canonical theory of gravity that builds spacetime out of fundamental spin networks in an attempt to reconcile general relativity with quantum mechanics. This leads to the prediction that space and time are discrete at the Planck scale ($\sim 10^{-35}m$). While significant technical details remain to be worked out, some desirable results have come out of the thoery. For instance, cosmological [2, 3] and black hole [4, 5, 6] solutions in LQG have been shown to exhibit singularity avoidance, an important test for any potential

theory of quantum gravity.

Over the last decade or so, a new quantization procedure known as polymerization has developed. In LQG, fundamental excitations turn out to be one-dimensional (rather like polymers) with three-dimensional space arising from a dense packing of discrete units viewed at macroscopic scales [7]. Polymerization is the analog of LQG in pure quantum mechanics, where a classically continuous space coordinate is quantized by allowing it to take on only a discrete set of values.

The equations involved in dynamical gravitational systems are frequently difficult to work with. Situations arise where an analytical solution cannot be found, or the solution is tedious and of an iterative nature, making for an insurmountable task by paper and pen. In these cases, computational methods often prove to be a useful tool, especially considering the natural way in which discrete systems may be written into code.

In this thesis we work with two separate Hamiltonian systems: a particle in the $1/r^2$ potential, and a massless scalar field in a spherically symmetric gravitational potential. In chapter 1 we apply polymer quantization as a method of singularity avoidance in the $1/r^2$ potential. In chapter 2, we explore black hole formation from the gravitational collapse of a massless scalar field in Painlevé-Gullstrand [8, 9] coordinates, notable for being regular across horizons. PG coordinates therefore allow us to continue beyond initial horizon formation (where other models tend to fail) and to see the black hole interior during evolution (which has not been done in any prior model) until the onset of singularity formation. We study this model both classically and in the presence of quantum corrections motivated by the polymer quantization in chapter 1. Computational methods prove invaluable for solving the equations in both chapters. A number of fascinating results emerge, the most dramatic being the disappearance of classical singularities.

Chapter 1

$1/r^2$ Potential

1.1 Introduction

A successful theory of quantum gravity is expected to provide a clear and unambiguous solution to the problems associated with the curvature singularities predicted by classical general relativity. This expectation is natural since quantum mechanics is known to cure classical singularities in other contexts, such as the hydrogen atom.

In recent years there has been much work suggesting that LQG [10] may indeed resolve gravitational singularities at least in the case of symmetry-reduced models, such as spatially homogeneous [2] and inhomogeneous [3] cosmologies and spherically symmetric black holes [4, 5, 6]. Given the simplifications that these models entail, it is pertinent to ask which features of the LQG quantization scheme are crucial to the observed singularity resolution.

There are two distinct, but related, features of the LQG quantization program that appear to play a role in achieving singularity resolution. The first is the fundamental discreteness that underlies LQG due to its focus on holonomies of connections and associated graphs embedded in a spatial manifold [11]. An analogous approach in a purely quantum mechanical

context is so-called polymer quantization [12, 13], in which the Hamiltonian dynamics occur on a discrete spatial lattice and the basic observables are the operators associated with location on the lattice and translation between lattice points. Polymer quantization provides a quantization scheme that is mathematically and physically distinct from Schrödinger quantization.

The second apparently key ingredient in the LQG singularity resolution mechanism is the regularization of the singular terms in the Hamiltonian using a trick first introduced in this context by Thiemann [11]. The regularization is achieved by first writing a classical inverse triad as the (singular) Poisson bracket of classical phase space functions whose quantum counterparts are known, and then defining the inverse triad operator as the commutator of these quantum counterparts. When applied to simple models this procedure gives rise to quantum operators with bounded spectra. The singularity is therefore kinematically "removed" from the spectra of relevant physical operators, such as the inverse scale factor.

One question that arises concerns the role or perhaps the necessity of the Thiemann trick in singularity resolution in LQG. Recall that in the case of the hydrogen atom the singularity resolution is achieved by defining self-adjoint operators in a Hilbert space. This requires a careful choice of boundary conditions on the wave function [14] but does not require modification of the singular $1/r$ potential. An example more relevant to quantum gravity is the reduced Schrödinger quantization of the "throat dynamics" of the Schwarzschild interior, which on imposition of suitable boundary conditions produced a discrete, bounded-from-below spectrum for the black hole mass [15].

Polymer quantization of the hydrogen atom was recently examined in [16], retaining only the s-wave (spherically symmetric) sector and regularizing the $1/r$ potential in a way that lets r take values on the whole real axis. The choice of symmetric versus antisymmetric boundary conditions at the singularity was found to have a signficant effect on the ground state even

after the singularity itself had been regularized. In particular, in the limit of small lattice separation the ground state eigenenergy showed evidence of convergence towards the ground state energy of the conventionally-quantized Schrödinger theory only for the antisymmetric boundary condition.

In this chapter, we perform a similar polymer quantization of the more singular $1/r^2$ potential. When the potential is regularized, we shall find that the choice of the boundary condition again has a significant effect on the lowest-lying eigenenergies. However, we shall also find that the polymer theory with the antisymmetric boundary condition is well defined even without regularizing the potential, and with this boundary condition the regularized and unregularized potentials yield closely similar spectra. The boundary condition at the singularity is hence not only a central piece of input in polymer quantization, but it can even provide, along with the modification to the kinetic term, the pivotal singularity avoidance mechanism. While this is expected from general arguments that we will make explicit later on, it is interesting and reassuring to see the mechanism work in the special case of the $1/r^2$ potential, whose degree of divergence is just at the threshold where a conventional Schrödinger quantization will necessarily result into a spectrum that is unbounded below. The polymer treatment of this system is thus turning a Hamiltonian that is unbounded below into one that has a well-defined ground state.

The $1/r^2$ potential is interesting in its own right: it has a classical scale invariance that is broken by the quantum theory. In addition, this potential appears frequently in black hole physics, for example in the near horizon and near singularity behaviour of the quasinormal mode potential [17, 18], in the near horizon behaviour of scalar field propagation [19] and in the Hamiltonian constraint in Painlevé-Gullstrand coordinates [20]. It may therefore conceivably be of direct relevance to quantum gravity. There is a substantial literature on Schrödinger quantization of this potential in $L_2(\mathbb{R}_+)$ (see for example [21, 22, 23, 24, 25, 26,

27] and the references in [28]), but we are not aware of previous work on polymer quantization of this potential.

The notation $L_2(\mathbb{R}, m(r)dr)$ defines the conditions met by the set of functions defining a Hilbert space. These functions are *square*-integrable (indicated by the subscript 2) with a positive-valued weight function $m(r)$ over the real line (indicated by $\mathbb{R}$). The inner product is defined in this case as

$$(\psi_1, \psi_2) = \int_{-\infty}^{\infty} m(r)\overline{\psi_1}\psi_2 dr. \tag{1.1.1}$$

It is possible, though not common in physics, to consider other spaces of functions which are not square-integrable. Also, we may generalize to other limits of integration such as the semi-positive real line $\mathbb{R}_+$. In some applications Hilbert spaces may be separated into sectors. For example, we may separate functions that satisfy symmetric boundary conditions from those which satisfy antisymmetric boundary conditions.

1.2 Schrödinger Quantization

We consider the classical Hamiltonian

$$H = p^2 - \frac{\lambda}{r^2}, \tag{1.2.1}$$

where the phase space is (r, p) with $r > 0$ and $\lambda \in \mathbb{R}$ is a constant. We shall take r, p and λ all dimensionless, and on quantization set $\hbar = 1$. If physical dimensions are restored, r and p will be expressed in terms of a single length scale but λ remains dimensionless. That the coupling constant is dimensionless is the speciality of a scale invariant potential.

Quantization of H (1.2.1) is of course subject to the usual ambiguities. In particular, if one views H as an effective Hamiltonian that comes from a higher-dimensional configuration

space via symmetry reduction, with r being a radial configuration variable, the appropriate Hilbert space may be $L_2(\mathbb{R}_+; m(r)dr)$. If for example $m(r) = r^a$, where $a \in \mathbb{R}$, then the ordering

$$\widehat{H} = -\left(\frac{\partial^2}{\partial r^2} + \frac{a}{r}\frac{\partial}{\partial r}\right) - \frac{\lambda}{r^2} \tag{1.2.2}$$

makes the quantum Hamiltonian $\widehat{H}$ symmetric. If the wave function in $L_2(\mathbb{R}_+; m(r)dr)$ is denoted by ψ, we may map ψ to $\widetilde{\psi} \in L_2(\mathbb{R}_+; dr)$ by $\widetilde{\psi}(r) = r^{a/2}\psi(r)$, and $\widehat{H}$ is then mapped in $L_2(\mathbb{R}_+; dr)$ to the Hamiltonian

$$\widehat{\widetilde{H}} = -\frac{\partial^2}{\partial r^2} - \frac{\widetilde{\lambda}}{r^2}, \tag{1.2.3}$$

where

$$\widetilde{\lambda} := \lambda - \frac{a}{2}\left(\frac{a}{2} - 1\right). \tag{1.2.4}$$

We shall consider any such mappings to have been done and take the quantum Hamiltonian to be simply

$$\widehat{H} = -\frac{\partial^2}{\partial r^2} - \frac{\lambda}{r^2}, \tag{1.2.5}$$

acting in the Hilbert space $L_2(\mathbb{R}_+; dr)$.

To guarantee that the time evolution generated by $\widehat{H}$ (1.2.5) is unitary, $\widehat{H}$ must be specified as a self-adjoint operator on $L_2(\mathbb{R}_+; dr)$ [29]. A comprehensive analysis of how to do this was given in [23] (see also [21, 22, 24, 25, 26, 27]). We shall review the results of [23] in a way that displays the spectrum explicitly for all the qualitatively different ranges of λ.

Before proceeding, we mention that several recent quantizations of the $1/r^2$ potential first regularize the potential using various renormalization techniques [24, 25, 26]. In particular, when the spectrum of a self-adjoint extension is unbounded below, these renormalization techniques need not lead to an equivalent quantum theory [27]. We shall here discuss only

the self-adjoint extensions.

To begin, recall [29] that the deficiency indices of $\widehat{H}$ are found by considering normalizable solutions to the eigenvalue equation

$$\widehat{H}\psi = \pm i\psi. \tag{1.2.6}$$

If we make the substitutions $\psi \to \sqrt{r}\omega$ and $\pm ir^2 \to z^2$, this reduces to Bessel's equation:

$$z^2\frac{\partial^2\omega}{\partial z^2} + z\frac{\partial\omega}{\partial z} + \left(z^2 - \kappa^2\right)\omega = 0, \tag{1.2.7}$$

where $\kappa^2 = 1/4 - \lambda$. As in [30], we use J and Y to denote Bessel functions of the first and second kind respectively. The normalizable solutions to (1.2.6) are linear combinations of $\sqrt{r}J_{\pm\kappa}(\sqrt{\pm i}r)$ when κ is not an integer. When κ is an integer, the linearly independant solutions are $\sqrt{r}J_{\kappa}(\sqrt{\pm i}r)$ and $\sqrt{r}Y_{\kappa}(\sqrt{\pm i}r)$. Since no normalizable solutions to (1.2.6) exist for $\lambda \leq -3/4$, there is a unique self-adjoint extension $\widehat{H}$ in this range of λ. For $\lambda > -3/4$, one family of normalizable linear combinations exists for each sign in (1.2.6), giving deficiency indices of $(1, 1)$. This implies that the solutions are paramatrized by an arbitrary phase. A boundary condition at $r = 0$ is needed to select this phase and make $\widehat{H}$ self-adjoint. Physically, this boundary condition will ensure that no probability is flowing in/out at $r = 0$.

1.2.1 $\lambda > 1/4$

For $\lambda > 1/4$, we write $\lambda = 1/4 + \alpha^2$ with $\alpha > 0$.

For $E > 0$, the linearly independent solutions to the eigenvalue equation

$$\widehat{H}\psi = E\psi \tag{1.2.8}$$

are $\sqrt{r}\, J_{\pm i\alpha}(\sqrt{E}\, r)$. These oscillate infinitely many times as $r \to 0$. To find the boundary condition, we consider the linear combinations

$$\psi_E(r) := \sqrt{r}\left[e^{i\beta}E^{-i\alpha/2}J_{i\alpha}(\sqrt{E}\, r) + e^{-i\beta}E^{i\alpha/2}J_{-i\alpha}(\sqrt{E}\, r)\right], \tag{1.2.9}$$

where β is a parameter that a priori could depend on E. As ψ_E is periodic in β with period 2π, and as replacing β by $\beta + \pi$ multiplies ψ_E by -1, we may understand β periodic with period π. For concreteness, we could choose for example $\beta \in [0, \pi)$.

For the probability flux through $r = 0$ to vanish, we need

$$\partial_t \int dr\, \overline{\psi_E}\psi_{E'} \to 0 \quad \text{as } r \to 0 \tag{1.2.10}$$

for all E and E', where the overline denotes the complex conjugate. Using the Schrödinger equation, this boils down to the requirement

$$\overline{\psi_E}\, \partial_r \psi_{E'} - \psi_{E'}\, \partial_r \overline{\psi_E} \to 0 \quad \text{as } r \to 0. \tag{1.2.11}$$

Using the small argument asymptotic form (equation (9.1.7) in [30])

$$J_\nu(z) \to \frac{(z/2)^\nu}{\Gamma(\nu+1)} \quad \text{as } z \to 0, \tag{1.2.12}$$

we find

$$\overline{\psi_E}\,\partial_r\psi_{E'} - \psi_{E'}\,\partial_r\overline{\psi_E} = 4\alpha|C|^2\sin(\beta-\beta') \quad \text{as } r\to 0 \tag{1.2.13}$$

where the constant

$$C := \frac{1}{2^{i\alpha}\Gamma(1+i\alpha)}. \tag{1.2.14}$$

This requires $\sin(\beta-\beta')=0$, and hence β must be independent of E. The choice of the phase β specifies the boundary condition at the origin.

To find the eigenvalues, we consider the solutions to (1.2.8). For $E>0$, the solutions are $\sqrt{r}J_{\pm i\alpha}(\sqrt{E}r)$, but these are not normalizable on $L_2(\mathbb{R}_+;dr)$. For $E<0$, the substitutions $\psi\to\sqrt{r}\omega$ and $-Er^2\to z^2$ put (1.2.8) into the form of the modified Bessel equation:

$$z^2\frac{\partial^2\omega}{\partial z^2} + z\frac{\partial\omega}{\partial z} - \left(z^2+\alpha^2\right)\omega = 0. \tag{1.2.15}$$

Two linearly independant solutions are given by $\sqrt{r}\,I_{i\alpha}(\sqrt{-E}\,r)$ and $\sqrt{r}\,K_{i\alpha}(\sqrt{-E}\,r)$, where I ad K are modified Bessel functions of the first and second kind respectively. The only normalizable solutions are $\sqrt{r}\,K_{i\alpha}(\sqrt{-E}\,r)$. These solutions must satisfy at $r\to 0$ the same boundary condition as ψ_E (1.2.9). Using C as defined above, and also defining

$$D := \frac{-\pi}{2\sinh(\alpha\pi)}, \tag{1.2.16}$$

the small r form of the solution for $E>0$ is

$$\psi_{E>0} = \sqrt{r}D\left(Cr^{i\alpha}e^{i\beta} + \overline{C}r^{-i\alpha}e^{-i\beta}\right). \tag{1.2.17}$$

The small argument asymptotic form needed for the $E<0$ solutions (equations (9.6.2) and

(9.6.7) in [30]) is

$$K_\nu(z) = K_{-\nu}(z) \to \frac{\pi}{\sin(\nu\pi)} \left[\frac{(z/2)^{-\nu}}{\Gamma(-\nu+1)} - \frac{(z/2)^{\nu}}{\Gamma(\nu+1)} \right] \quad \text{as } z \to 0. \tag{1.2.18}$$

This gives

$$\psi_{E<0} = \sqrt{r} D \left[-C r^{i\alpha} (-E)^{\frac{i\alpha}{2}} + \overline{C} r^{-i\alpha} (-E)^{\frac{i\alpha}{2}} \right]. \tag{1.2.19}$$

Since $\psi_{E<0}$ must satisfy the same boundary condition as $\psi_{E>0}$, we compare the square of these functions and find the eigenvalues to be

$$E_n = E_0 \exp(-2\pi n/\alpha), \quad n \in \mathbb{Z}, \tag{1.2.20}$$

where

$$E_0 = -\exp[(2\beta + \pi)/\alpha]. \tag{1.2.21}$$

This spectrum is an infinite tower, with $E_n \to 0_-$ as $n \to \infty$ and $E_n \to -\infty$ as $n \to -\infty$. The spectrum is unbounded from below.

We note that Schrödinger quantization of a regulated form of the potential yields a semi-infinite tower of states that is similar to (1.2.20) as $n \to \infty$ but has a ground state [25]. The energy of the ground state goes to $-\infty$ when the regulator is removed.

1.2.2 $\lambda = 1/4$

For $\lambda = 1/4$, the solutions to the eigenvalue equation (1.2.8) for $E > 0$ are $\sqrt{r}\, J_0(\sqrt{E}\, r)$ and $\sqrt{r}\, Y_0(\sqrt{E}\, r)$. We consider the linear combinations

$$\psi_E(r) := \sqrt{r} \left\{ (\cos\beta) J_0(\sqrt{E}\, r) + (\sin\beta) \left[\frac{\pi}{2} Y_0(\sqrt{E}\, r) - \ln\left(\frac{\sqrt{E}\, e^{\gamma}}{2} \right) J_0(\sqrt{E}\, r) \right] \right\}, \tag{1.2.22}$$

where γ is Euler's constant and β is again a parameter that may be understood periodic with period π and could a priori depend on E. As above, we find that β must be a constant independent of E and its value determines the boundary condition at the origin.

Normalizable solutions to (1.2.8) exist only for $E < 0$. They are $\sqrt{r}\, K_0(\sqrt{-E}\, r)$, and they must satisfy the same boundary condition as ψ_E (1.2.22) at $r \to 0$. Using the small argument expansion of K_0 (equations (9.6.12) and (9.6.13) in [30])

$$K_0(z) = -\left[\ln\left(\frac{z}{2}\right) + \gamma \right] I_0(z) + \frac{\frac{1}{4}z^2}{(1!)^2} + \left(1 + \frac{1}{2}\right) \frac{(\frac{1}{4}z^2)^2}{(2!)^2} + \left(1 + \frac{1}{2} + \frac{1}{3}\right) \frac{(\frac{1}{4}z^3)^2}{(3!)^2} + \cdots, \tag{1.2.23}$$

where

$$I_0(z) = 1 + \frac{\frac{1}{4}z^2}{(1!)^2} + \frac{(\frac{1}{4}z^2)^2}{(2!)^2} + \frac{(\frac{1}{4}z^2)^3}{(3!)^2} + \cdots, \tag{1.2.24}$$

we find that for $\beta = 0$ there are no normalizable states, while for $0 < \beta < \pi$ there is exactly one normalizable state, with the energy

$$E_0 = -4 \exp(-2\gamma + 2\cot\beta). \tag{1.2.25}$$

1.2.3 $-3/4 < \lambda < 1/4$

For $-3/4 < \lambda < 1/4$, we write $\lambda = 1/4 - \nu^2$ with $0 < \nu < 1$.

The solutions to the eigenvalue equation (1.2.8) for $E > 0$ are $\sqrt{r}\, J_{\pm\nu}(\sqrt{E}\, r)$. Considering the linear combinations

$$\psi_E(r) := \sqrt{r}\left[(\cos\beta)E^{-\nu/2}J_\nu(\sqrt{E}\, r) + (\sin\beta)E^{\nu/2}J_{-\nu}(\sqrt{E}\, r)\right], \tag{1.2.26}$$

we find as above that β is a constant, understood periodic with period π, and its value specifies the boundary condition at the origin.

Normalizable solutions to (1.2.8) exist only for $E < 0$. They are $\sqrt{r}\, K_\nu(\sqrt{-E}\, r)$ and must satisfy the same boundary condition as ψ_E (1.2.26) at $r \to 0$. Using the small argument asymptotic form of K_ν [30], we find that there are no normalizable states for $0 \le \beta \le \pi/2$, while for $\pi/2 < \beta < \pi$ there is exactly one normalizable state, with the energy

$$E_0 = -(-\cot\beta)^{1/\nu}. \tag{1.2.27}$$

We note that in the special case of a free particle, $\lambda = 0$, the Bessel functions reduce to trigonometric and exponential functions.

1.2.4 $\lambda \le -3/4$

For $\lambda \le -3/4$, we write $\lambda = 1/4 - \nu^2$ with $\nu \ge 1$. $\widehat{H}$ is now essentially self-adjoint (there are no free parameters to be specified). Any prospective normalizable solution to (1.2.8) would need to have $E < 0$ and take the form $\sqrt{r}\, K_\nu(\sqrt{-E}\, r)$, but since now $\nu \ge 1$, these solutions are not normalizable and hence do not exist.

1.3 Polymer Quantization

In this section we develop the polymer quantization of the $1/r^2$ potential We proceed as in [16], briefly reiterating the main steps for completeness.

It is necessary to extend the r coordinate to negative values with the replacement $r \to x \in \mathbb{R}$ in order to use finite difference schemes at the origin. This will allow us to introduce at the origin both a symmetric boundary condition (with the regulated potential developed in subsection 1.3.2) and an antisymmetric boundary condition.

The polymer Hilbert space on the full real line is spanned by the basis states

$$\psi_{x_0}(x) = \begin{cases} 1, & x = x_0 \\ 0, & x \neq x_0 \end{cases} \tag{1.3.1}$$

with the inner product

$$(\psi_x, \psi_{x'}) = \delta_{x,x'}, \tag{1.3.2}$$

where the object on the right hand side is the Kronecker delta. The position operator acts by multiplication as

$$(\hat{x}\psi)(x) = x\psi(x). \tag{1.3.3}$$

Defining a momentum operator takes more care. Consider the translation operator $\widehat{U}$, which acts as

$$(\widehat{U}_\mu \psi)(x) = \psi(x + \mu). \tag{1.3.4}$$

In ordinary Schrödinger quantization we would have $\widehat{U}_\mu = e^{i\mu\hat{p}}$. Following [12], we hence

define the momentum operator and its square as

$$\hat{p} = \frac{1}{2i\bar{\mu}}(\widehat{U}_{\bar{\mu}} - \widehat{U}_{\bar{\mu}}^{\dagger}), \tag{1.3.5a}$$

$$\widehat{p^2} = \frac{1}{\mu^2}(2 - \widehat{U}_{\mu} - \widehat{U}_{\mu}^{\dagger}), \tag{1.3.5b}$$

where $\bar{\mu} := \mu/2$. We may thus write the polymer Hamiltonian as

$$\widehat{H}_{\rm pol} = \widehat{T}_{\rm pol} + \widehat{V}_{\rm pol} \ , \tag{1.3.6}$$

where

$$\widehat{T}_{\rm pol} = \frac{1}{\mu^2}(2 - \widehat{U}_{\mu} - \widehat{U}_{\mu}^{\dagger}), \tag{1.3.7a}$$

$$\widehat{V}_{\rm pol} = -\frac{\lambda}{\hat{x}^2}. \tag{1.3.7b}$$

Considering the action of $\hat{x}$ and $\widehat{U}_{\mu}$, we see that the dynamics generated by (1.3.6) separates the polymer Hilbert space into an infinite number of superselection sectors, each having support on a regular μ-spaced lattice $\{\Delta + n\mu \mid n \in \mathbb{Z}\}$. The choice of $\{\Delta \mid 0 \leq \Delta < \mu\}$ picks the sector. Since we wish to study singularity resolution, we concentrate on the $\Delta = 0$ sector, which we expect the singularity of the potential to affect most. We shall discuss the regularization of $\widehat{V}_{\rm pol}$ at this singularity in subsection 1.3.2.

1.3.1 Semiclassical Polymer Theory

Before analyzing the full polymer quantum theory, we examine the semiclassical polymer spectrum using the Bohr-Sommerfeld quantization condition.

Following [2, 5, 6], we take the classical limit of the polymer Hamiltonian (1.3.6) by

keeping the polymerization scale μ fixed and making the replacement $\widehat{U}_\mu \to e^{i\mu p}$, where p is the classical momentum. Note that this is different from the continuum limit in which μ goes to zero and the quantum theory is expected to be equivalent to Schrödinger quantization [31].

We assume $\lambda > 0$. It follows, as will be verified below, that the classical polymer orbits never reach the origin, and we may hence assume the configuration variable x to be positive and revert to the symbol r. The classical polymer Hamiltonian takes thus the form

$$H_{\rm pol} = \frac{\sin^2(\bar{\mu}p)}{\bar{\mu}^2} - \frac{\lambda}{r^2}. \tag{1.3.8}$$

Note that $H_{\rm pol}$ reduces to the classical non-polymerized Hamiltonian (1.2.1) in the limit $\bar{\mu} \to 0$.

A first observation is that the kinetic term in $H_{\rm pol}$ is non-negative and bounded above by $1/\bar{\mu}^2$. Denoting the time-independent value of $H_{\rm pol}$ on a classical solution by E, it follows that E is bounded above by

$$E < E_{\rm max} := \frac{1}{\bar{\mu}^2}. \tag{1.3.9}$$

Looking into the dynamics, we find

$$\dot{x} = \frac{2}{\bar{\mu}} \cos(\bar{\mu}p) \sin(\mu p), \tag{1.3.10}$$

indicating possible turning points where either the cosine or the sine term are zero. For $E > 0$, the only (real) turning point is

$$r_- := \left(\frac{\lambda \bar{\mu}^2}{1 - \bar{\mu}^2 E} \right)^{1/2}. \tag{1.3.11}$$

and the solution is a scattering solution, with $r \to \infty$ as $t \to \pm\infty$. For $E < 0$ we find an additional turning point:

$$r_+ := \left(\frac{\lambda}{-E}\right)^{1/2}, \tag{1.3.12}$$

and the solution is a bound solution, with r oscillating periodically between r_+ and r_-. Note that r_+ is independent of $\bar{\mu}$, and the outer turning point in fact coincides with the turning point of the non-polymerized classical theory.

The classical polymer solutions are thus qualitatively similar to the classical non-polymerized solutions at large r, both for $E \geq 0$ and for $E < 0$. What is different is that the polymer energy is bounded from above, and more importantly that the polymer solutions bounce at $r = r_-$. In this sense the classical polymer theory has resolved the singularity at $r = 0$. The resolution depends on the polymerization scale: for fixed E, $r_- = \bar{\mu}\sqrt{\lambda}\big[1 + \mathbb{O}(\bar{\mu}^2)\big] \to 0$ as $\bar{\mu} \to 0$, and for fixed $\bar{\mu}$, $r_- \to \bar{\mu}\sqrt{\lambda}$ as $E \to 0$.

As the $E < 0$ solutions are periodic, we can use the Bohr-Sommerfeld quantization condition to estimate the semiclassical quantum spectrum. A subtlety here is that semiclassical estimates already in ordinary Schrödinger quantization with a $1/r^2$ term involve a shift in the coefficient of this term [32]. Anticipating a similar shift here, we look at the Bohr-Sommerfeld quantization condition with λ replaced by λ_{eff}, and we will then determine λ_{eff} by comparison with the Schrödinger quantization.

For a classical solution with given E, formula (1.3.8) implies (with λ replaced by λ_{eff})

$$r = \frac{\bar{\mu}\sqrt{\lambda_{\text{eff}}}}{\sqrt{\sin^2(\bar{\mu}p) - \bar{\mu}^2 E}}. \tag{1.3.13}$$

Taking $E < 0$, the phase space integral $J(E) := \oint r\, dp$ over a full cycle is hence

$$\begin{aligned} J(E) &= \oint r\, dp \\ &= 2\sqrt{\lambda_{\text{eff}}} \int_0^{\pi/(2\bar{\mu})} \frac{\bar{\mu}\, dp}{\sqrt{\sin^2(\bar{\mu}p) - \bar{\mu}^2 E}} \qquad (p = y/\bar{\mu}) \\ &= 2\sqrt{\lambda_{\text{eff}}} \int_0^{\pi/2} \frac{dy}{\sqrt{\sin^2(y) - \bar{\mu}^2 E}}. \\ &= \frac{2\sqrt{\lambda_{\text{eff}}}}{\sqrt{1-\bar{\mu}^2 E}} \int_0^{\pi/2} \frac{dy}{\sqrt{1 - (1-\bar{\mu}^2 E)^{-1} \cos^2(y)}} \\ &= \frac{2\sqrt{\lambda_{\text{eff}}}}{\sqrt{1-\bar{\mu}^2 E}}\, K\left((1-\bar{\mu}^2 E)^{-1/2} \right), \end{aligned} \tag{1.3.14}$$

where K is the complete elliptic integral of the first kind [33]. In the limit $\bar{\mu}^2 E \to 0$, the expansion (8.113.3) in [33] yields

$$J(E) = 2\sqrt{\lambda_{\text{eff}}} \left[\ln\left(\frac{4}{\bar{\mu}\sqrt{-E}} \right) + \mathbb{O}\left(\bar{\mu}\sqrt{-E} \right) \right]. \tag{1.3.15}$$

The Bohr-Sommerfeld quantization condition now states that the eigenenergies of the highly excited states are given asymptotically by $J(E) = 2\pi n$, where $n \gg 1$ is an integer. By (1.3.15), this gives the asymptotic eigenenergies

$$E_n = -\frac{16}{\bar{\mu}^2} \exp\bigl(-2\pi n/\sqrt{\lambda_{\text{eff}}}\bigr), \quad n \to \infty. \tag{1.3.16}$$

The Bohr-Sommerfeld estimate (1.3.16) agrees with the spectrum (1.2.20) obtained from conventional Schrödinger quantization for $\lambda > 1/4$, provided $\lambda_{\text{eff}} = \lambda - \frac{1}{4}$ and we choose in

(1.2.20) the self-adjoint extension for which

$$\beta = -\frac{\pi}{2} + \alpha \ln(4/\bar{\mu}) \pmod{\pi}. \tag{1.3.17}$$

The shift $\lambda_{\text{eff}} = \lambda - \frac{1}{4}$ is exactly that which arises in ordinary Schrödinger quantization of potentials that include a $1/r^2$ term: the reason there is the matching of the small r behaviour of the exact eigenstates to the WKB approximation. For a lucid analysis of this phenomenon in the quasinormal mode context, see the discussion between equations (23) and (28) in [32]. Note, however, that in our system the Bohr-Sommerfeld condition cannot be applied directly to the unpolymerized theory, since $J(E)$ (1.3.14) diverges as $\bar{\mu} \to 0$.

1.3.2 Full Quantum Polymer Theory

We now return to the full polymer quantum theory, with the Hamiltonian (1.3.6) and $\lambda \in \mathbb{R}$.

We write the basis states in Dirac notation as $|m\mu\rangle$, where $m \in \mathbb{Z}$. Writing a state in this basis as $\psi = \sum_m c_m |m\mu\rangle$, it follows from (1.3.2) that the inner product reads $\left(\psi^{(1)}, \psi^{(2)}\right) = \sum_m \overline{c_m{}^{(1)}}\, c_m^{(2)}$. The Hilbert space is thus $L_2(\mathbb{Z})$. It will be useful to decompose this Hilbert space as the direct sum $L_2(\mathbb{Z}) = L_2^s(\mathbb{Z}) \oplus L_2^a(\mathbb{Z})$, where the states in the symmetric sector $L_2^s(\mathbb{Z})$ satisfy $c_m = c_{-m}$ and the states in the antisymmetric sector $L_2^a(\mathbb{Z})$ satisfy $c_m = -c_{-m}$.

The action of $\widehat{T}_{\text{pol}}$ (1.3.7a) reads

$$\widehat{T}_{\text{pol}} \left(\sum_m c_m |m\mu\rangle \right) = \frac{1}{\mu^2} \sum_m \left(2c_m - c_{m+1} - c_{m-1}\right) |m\mu\rangle \,. \tag{1.3.18}$$

$\widehat{T}_{\text{pol}}$ is clearly a manifestly symmetric, bounded operator on $L_2(\mathbb{Z})$. An explicit solution of the eigenvalue equation $\widehat{T}_{\text{pol}}\psi = E\psi$, given in equation (1.3.32) below, shows that there are no normalizable solutions with $E = \pm i$. $\widehat{T}_{\text{pol}}$ is hence essentially self-adjoint ([34], Theorem

X.2). It is also positive, since $\left(\psi, \widehat{T}_{\rm pol}\psi\right) = |\hat{p}\psi|^2 > 0$ for any $\psi \neq 0$.

The action of $\widehat{V}_{\rm pol}$ (1.3.7b) reads

$$\widehat{V}_{\rm pol}\left(\sum_m c_m \left|m\mu\right\rangle\right) = -\frac{\lambda}{\mu^2}\sum_m f_m^{\rm pol}\, c_m \left|m\mu\right\rangle, \tag{1.3.19}$$

where

$$f_m^{\rm pol} := \frac{1}{m^2}. \tag{1.3.20}$$

As (1.3.19) is ill-defined on any state for which $c_m \neq 0$, $\widehat{V}_{\rm pol}$ is not a densely-defined operator on $L_2(\mathbb{Z})$. We consider two ways to handle this singularity.

The first way is to regulate $\widehat{V}_{\rm pol}$ explicitly. For $x \in \mathbb{R} \setminus \{0\}$ we can write

$$\frac{\mathrm{sgn}(x)}{\sqrt{|x|}} = 2\frac{d(\sqrt{|x|})}{dx}, \tag{1.3.21}$$

and on our lattice this can be implemented as a finite difference expression. It is important to use central rather than forward or backward differences; forward differences do not work well for dynamics moving in from behind, and the opposite case is problematic for backward differences. The central difference derivative is given by

$$\frac{\mathrm{sgn}(x)}{\sqrt{|x|}} \to \frac{1}{\mu}\left(\sqrt{|x_{m+1}|} - \sqrt{|x_{m-1}|}\right) + \mathbb{O}(\mu^2). \tag{1.3.22}$$

We hence define the regulated polymer version of $\mathrm{sgn}(x)/\sqrt{|x|}$ by dropping the $\mathbb{O}(\mu^2)$ term in (1.3.22), and we define the regulated polymer potential $\widehat{V}_{\rm pol}^{\rm reg}$ by raising this to the fourth power,

$$\frac{\lambda}{(x_m)^2} \to \frac{\lambda}{\mu^4}\left(\sqrt{|x_{m+1}|} - \sqrt{|x_{m-1}|}\right)^4. \tag{1.3.23}$$

The action of the regularized potential is

$$\widehat{V}_{\rm pol}^{\rm reg}\left(\sum_m c_m\,|m\mu\rangle\right) = -\frac{\lambda}{\mu^2}\sum_m f_m^{\rm reg}\,c_m\,|m\mu\rangle\,, \tag{1.3.24}$$

where

$$f_m^{\rm reg} := \left(\sqrt{|m+1|} - \sqrt{|m-1|}\right)^4. \tag{1.3.25}$$

$\widehat{V}_{\rm pol}^{\rm reg}$ is clearly a bounded essentially self-adjoint operator on $L_2(\mathbb{Z})$, and its operator norm is $4|\lambda|/(\mu^2)$.

The regulated polymer Hamiltonian can now be defined by

$$\widehat{H}_{\rm pol}^{\rm reg} = \widehat{T}_{\rm pol} + \widehat{V}_{\rm pol}^{\rm reg}. \tag{1.3.26}$$

It follows by the Kato-Rellich theorem ([34], Theorem X.12) that $\widehat{H}_{\rm pol}^{\rm reg}$ is essentially self-adjoint on $L_2(\mathbb{Z})$ and bounded below by $-4|\lambda|/(\mu^2)$. Further, both $\widehat{T}_{\rm pol}$ and $\widehat{V}_{\rm pol}^{\rm reg}$ leave $L_2^s(\mathbb{Z})$ and $L_2^a(\mathbb{Z})$ invariant, and their boundedness and self-adjointness properties mentioned above hold also for their restrictions to $L_2^s(\mathbb{Z})$ and $L_2^a(\mathbb{Z})$. It follows that $\widehat{H}_{\rm pol}^{\rm reg}$ restricts to both $L_2^s(\mathbb{Z})$ and $L_2^a(\mathbb{Z})$ as a self-adjoint operator bounded below by $-4|\lambda|/(\mu^2)$. We denote both of these restrictions by $\widehat{H}_{\rm pol}^{\rm reg}$, leaving the the domain to be understood from the context.

The second way to handle the singularity of $\widehat{V}_{\rm pol}$ (1.3.19) is to restrict at the outset to the antisymmetric subspace $L_2^a(\mathbb{Z})$, where $\widehat{V}_{\rm pol}$ is essentially self-adjoint and its operator norm is $|\lambda|/(\mu^2)$. It follows as above that the unregulated polymer Hamiltonian

$$\widehat{H}_{\rm pol} = \widehat{T}_{\rm pol} + \widehat{V}_{\rm pol} \tag{1.3.27}$$

on $L_2^a(\mathbb{Z})$ is essentially self-adjoint and bounded below by $-|\lambda|/(\mu^2)$.

Two comments are in order. First, $\widehat{H}_{\rm reg}$ can be written in terms of operators as

$$\widehat{H}_{\rm reg} = \frac{1}{\mu^2}(2 - \widehat{U}_\mu - \widehat{U}_\mu^\dagger) - \frac{\lambda}{\mu^4}\left(\widehat{U}_\mu\sqrt{|\hat{x}|}\widehat{U}_\mu^\dagger - \widehat{U}_\mu^\dagger\sqrt{|\hat{x}|}\widehat{U}_\mu\right)^4. \tag{1.3.28}$$

The potential in (1.3.28) can hence be viewed as arising from the substitution

$$\frac{\mathrm{sgn}(x)}{\sqrt{|x|}} \to \frac{1}{i\mu}U_\mu^\dagger\left\{\sqrt{|x|}, U_\mu\right\} - \frac{1}{i\mu}U_\mu\left\{\sqrt{|x|}, U_\mu^\dagger,\right\}, \tag{1.3.29}$$

in place of (1.3.21), where $U_\mu = e^{i\mu p}$ is the classical function corresponding to the quantum translation operator. Similarly to Thiemann's regularization of inverse triad operators in loop quantum gravity [11], the right hand side of this equation becomes regular upon the replacement of classical functions and Poisson brackets with their quantum counterparts. Note that (1.3.29) is symmetric by definition, which corresponds to the use of central differences in (1.3.22).

Second, the regulated potential vanishes at the origin but is greater in absolute value than the unregulated potential for $|m| \geq 1$. However, the difference is significant only for the lowest few $|m|$, and the two potentials quickly converge as $|m| \to \infty$ (see Fig. 1.1). The regulated and unregulated potentials hence differ significantly only near the singularity.

1.3.3 Eigenstates and the Numerical Method

We are now ready to look for the eigenstates of the Hamiltonian. Writing the eigenstate as $\psi = \sum_m c_m |m\mu\rangle$ and denoting the eigenvalue by E, the regulated eigenvalue equation $\widehat{H}^{\rm reg}_{\rm pol}\psi = E\psi$ and the unregulated eigenvalue equation $\widehat{H}_{\rm pol}\psi = E\psi$ both give a recursion

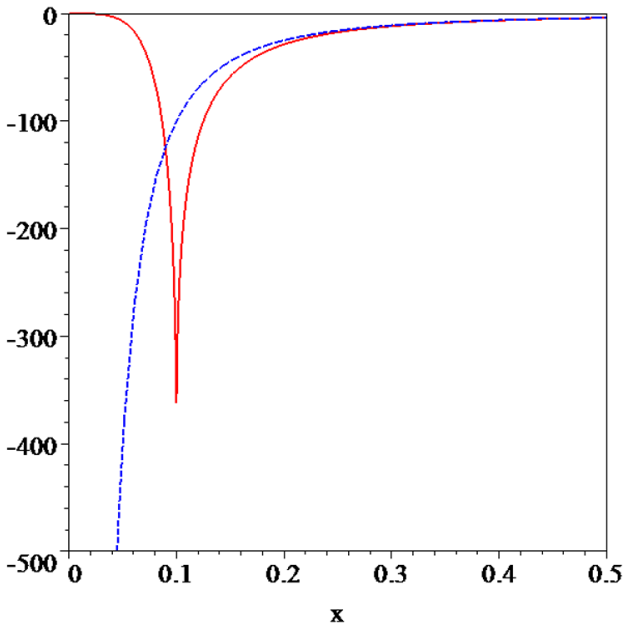

Figure 1.1: The solid (red) line is the regulated $-1/x^2$ potential ($\lambda = 1$, $\mu = 0.1$). The dashed (blue) line is the unregulated potential.

relation that takes the form

$$c_m \left(2 - \mu^2 E - \lambda f_m\right) = c_{m+1} + c_{m-1}, \tag{1.3.30}$$

where $f_m = f_m^{\text{reg}}$ (1.3.25) for the regulated potential and $f_m = f_m^{\text{pol}}$ (1.3.20) for the unregulated potential. Note that the polymerization scale μ enters this recursion relation only in the combination $\mu^2 E$, whether or not the potential is regulated. This is a direct consequence of the scale invariance of the potential.

From now on, we take $\lambda > 0$ and $E < 0$.

We use the "shooting method" that was applied in [16] to the polymerized $1/|x|$ potential.

For large $|m|$, (1.3.30) is approximated by

$$c_m \left(2 - \mu^2 E\right) = c_{m+1} + c_{m-1}. \tag{1.3.31}$$

The linearly independent solutions to (1.3.31) are

$$c_m = \left[1 - \frac{\mu^2 E}{2} + \sqrt{\left(1 - \frac{\mu^2 E}{2}\right)^2 - 1}\right]^{\pm m}. \tag{1.3.32}$$

The upper (respectively lower) sign gives coefficients that increase (decrease) exponentially as $m \to \infty$. We can therefore use (1.3.32) with the lower sign to set the initial conditions at large positive m [35].

To set up the shooting problem, we choose a value for $\mu^2 E$ and begin with some $m_0 \gg \sqrt{\frac{\lambda}{\mu^2 |E|}}$ to find c_{m_0} and $c_{m_0 - 1}$ using the approximation (1.3.32). We then iterate downwards with (1.3.30). In the antisymmetric sector, we stop the iteration at c_0 and shoot for values of $\mu^2 E$ for which $c_0 = 0$. This shooting problem is well defined both for the unregulated potential (1.3.19) and for the regulated potential (1.3.24), since the computation of c_0 via (1.3.30) does not require evaluation of f_m at $m = 0$. In the symmetric sector, we stop at the iteration at c_{-1} and shoot for values of $\mu^2 E$ for which $c_{-1} = c_1$. As the computation of c_{-1} requires evaluation of f_m at $m = 0$, the symmetric sector is well defined only for the regulated potential.

1.4 Results

We shall now compare the spectra of full polymer quantization, Bohr-Sommerfeld polymer quantization and ordinary Schrödinger quantization. We are particularly interested in the

sensitivity of the results to the choice of the symmetric versus the antisymmetric sector.

First of all, we find that when the potential is regulated, the choice of the symmetric versus antisymmetric boundary condition in the full polymer quantum theory has no significant qualitative effect for sufficiently large λ, the only difference being slightly lower eigenvalues for the symmetric boundary condition. The lowest five eigenvalues in the two sectors are shown in Table 1.1 for $\lambda = 2$. This is in a sharp contrast with what was found in [16] for the $1/r$ potential, where the symmetric sector contained a low-lying eigenvalue that appeared to tend to $-\infty$ as the polymerization scale was decreased.

	antisymmetric	symmetric
E_0	-6.14	-6.37
E_1	$-2.35 \cdot 10^{-2}$	$-2.43 \cdot 10^{-2}$
E_2	$-2.03 \cdot 10^{-4}$	$-2.10 \cdot 10^{-4}$
E_3	$-1.76 \cdot 10^{-6}$	$-1.82 \cdot 10^{-6}$
E_4	$-1.52 \cdot 10^{-8}$	$-1.57 \cdot 10^{-8}$

Table 1.1: The lowest five eigenvalues of the regulated potential with antisymmetric and symmetric boundary conditions ($\lambda = 2$, $\mu = 1$).

Another key feature is that for sufficiently large λ there is indeed a negative energy ground state. For $3 \leq \lambda \leq 4$, the plots of the lowest eigenvalues as a function of λ in Fig. 1.2 show that the analytic lower bound obtained in subsection 1.3.2 is accurate within a factor of 1.2 for the regulated potential in the antisymmetric sector and within a factor of two for the unregulated potential.

Figure 1.2 also indicates that the lowest eigenvalues converge towards zero as λ decreases, for both the unregulated and regulated potentials, with the unregulated eigenvalues reaching zero slightly before the regulated. Near $E_n = 0$ the relationship is quadratic in λ while the plots straighten out to a linear relationship for larger λ.

The numerics become slow as the energies are close to zero. We were unable to inves-

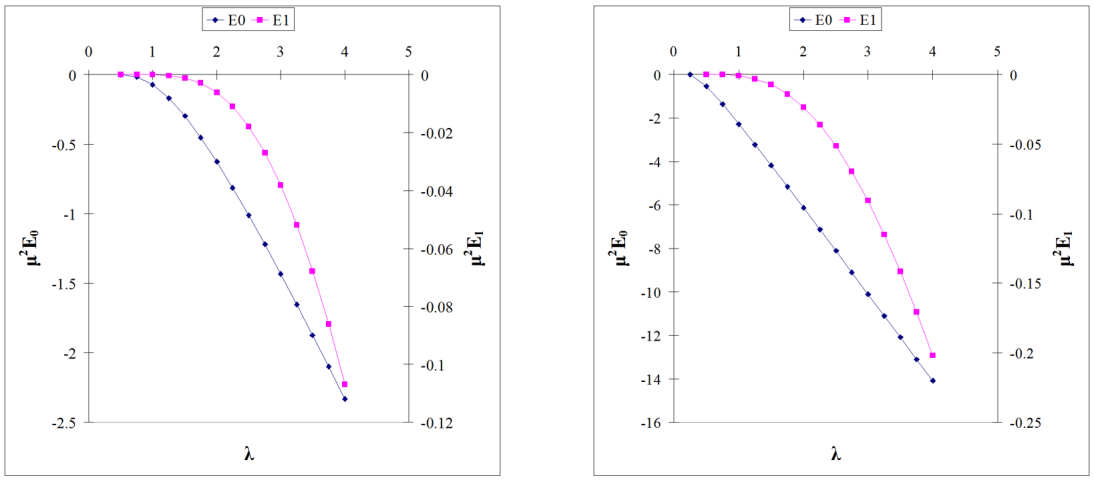

(a) The unregulated potential with antisymmetric boundary conditions.

(b) The regulated potential with antisymmetric boundary conditions.

Figure 1.2: The lowest two energy levels as a function of λ.

tigate systematically whether bound states exist for $\lambda \leq 1/4$, and in particular to make a comparison with the single bound state that occurs in Schrödinger quantization with certain self-adjoint extensions. For λ slightly below $1/4$, we do find one bound state, but we do not know whether the absence of further bound states is a genuine property of the system of an artifact of insufficient computational power. This would be worthy of further investigation. The eigenvalues show a similar dependence on λ for both regulated and unregulated potentials, with the energies for the regulated potential being lower than those for the unregulated version as one would expect from comparing the potentials as in Fig. 1.1.

For $\lambda > 1/4$, we find that the eigenvalues E_n depend on n exponentially, except for the lowest few eigenvalues ($n = 0, 1$). The coefficient in the exponent is in close agreement with the exact Schrödinger spectrum (1.2.20) and with the Bohr-Sommerfeld polymer spectrum (1.3.16) with $\lambda_{\text{eff}} = \lambda - 1/4$. Representative spectra are shown as semi-log plots in Fig. 1.3, where the linear fit is computed using only the points with $n \geq 2$. By matching the linear fit to the Schrödinger spectrum (1.2.20) and reading off the self-adjointness parameter β,

we can determine the self-adjoint extension of the Schrödinger Hamiltonian that matches the polymer theory for the highly-excited states. The results shown in Fig. 1.4 indicate that the self-adjoint parameter β depends linearly on the coupling parameter α, and the slope in this relation is within 10 per cent of the slope obtained from the Bohr-Sommerfeld estimate (1.3.17), $\ln 8 \approx 2.0794$ (for $\mu = 1$, $\bar{\mu} = 1/2$).

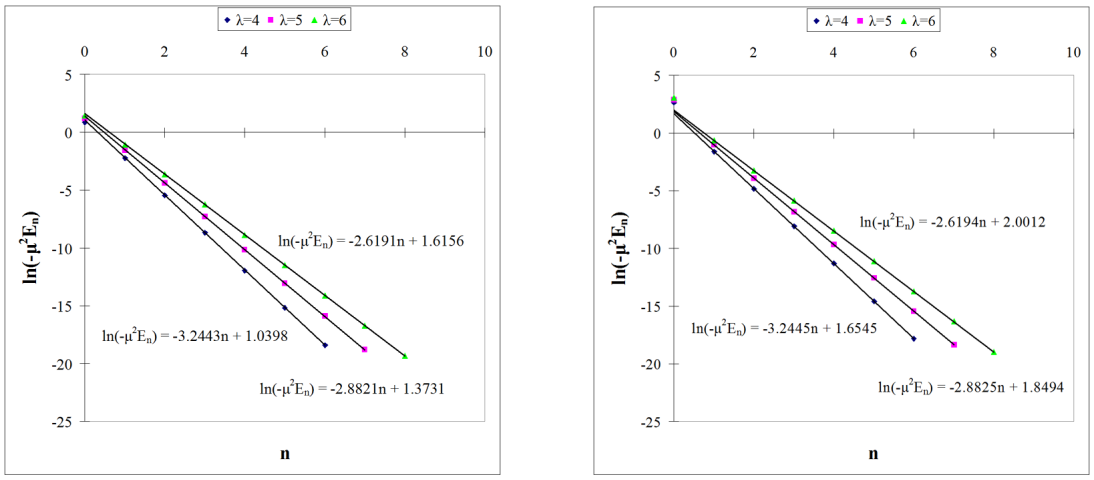

(a) The unregulated potential with antisymmetric boundary conditions.

(b) The regulated potential with antisymmetric boundary conditions.

Figure 1.3: $\ln(-\mu^2 E_n)$ vs. n with linear fits ($R^2 = 1$).

Finally, our numerical eigenvalues E_n are in excellent agreement with the analytic approximation scheme of [20], provided this scheme is understood as the limit of large λ with fixed n. If the numerical results shown in Fig. 1.3 are indicative of the complementary limit of large n with fixed λ, they show that the approximation scheme of [20] does not extend to this limit.

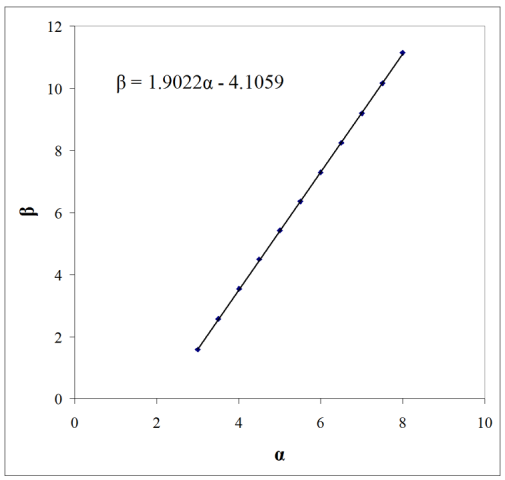

(a) The unregulated potential with antisymmetric boundary conditions.

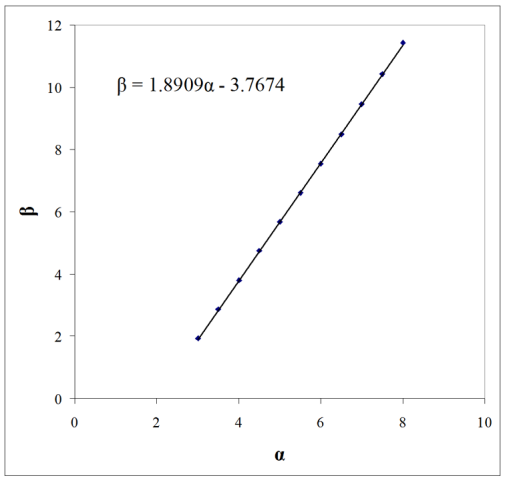

(b) The regulated potential with antisymmetric boundary conditions.

Figure 1.4: Plots of β vs. α for $\mu = 1$ with a linear fit ($R^2 = 1$).

1.5 Conclusions

We have compared Schrödinger and polymer quantizations of the $1/r^2$ potential on the positive real line. The broad conclusion is that these quantization schemes are in excellent agreement for the highly-excited states and differ significantly only for the low-lying states. In particular, the polymer spectrum is bounded below, whereas the Schrödinger spectrum is known to be unbounded below when the coefficient of the potential term is sufficiently negative. We also find that the Bohr-Sommerfeld semiclassical quantization condition reproduces correctly the distribution of the highly-excited polymer eigenvalues. At some level this agreement is not surprising, since one expects that for any mathematically consistent quantization scheme, in some appropriate large n, semiclassical limit, the spectra should agree. For antisymmetric boundary conditions both Schrödinger and regulated and unregulated polymer quantizations obey the criteria, so it is perhaps not surprising that they agree at least for energies close to zero. It is somewhat surprising that they agree so well for low

n (where "low" is in the context of the polymer spectra which are bounded below).

A central conceptual point was the regularization of the classical $r = 0$ singularity in the polymer theory. We did this first by explicitly regulating the potential, using a finite differencing scheme that mimics the Thiemann trick used with the inverse triad operators in LQG [11]: this method allows a choice of either symmetric or antisymmetric boundary conditions at the origin. We then observed, as prevously noted in [20], that the singularity can alternatively be handled by leaving the potential unchanged but just imposing the antisymmetric boundary condition at the origin. The numerics showed that all three of these options gave very similar spectra, and the agreement was excellent for the highly-excited states.

To what extent is the agreement of these three regularization options specific to the $1/r^2$ potential? Consider the polymer quantization of the Coulomb potential, $-1/r$. When the Coulomb potential is explicitly regulated, it was shown in [16] that the choice between the symmetric and antisymmetric boundary conditions makes a significant difference for the ground state energy. We have now computed numerically the lowest five eigenenergies for the unregulated $-1/r$ potential with the antisymmetric boundary condition, with the results shown in Table 1.2. Comparison with the results in [16] shows that the regularization of the potential makes no significant difference with the antisymmetric boundary condition. As noted in [16], for sufficiently small lattice spacing the antisymmetric boundary condition spectrum tends to that which is obtained in Schrödinger quantization with the conventional hydrogen s-wave boundary condition [14].

We conclude that in polymer quantization of certain singular potentials, a suitably-chosen boundary condition suffices to produce a well-defined and arguably physically acceptable quantum theory, without the need to explicitly modify the classical potential near its singularity: the antisymmetric boundary condition effectively removes the $r = 0$ eigenstate from

n	E_n
0	-0.250
1	-0.0625
2	-0.0278
3	-0.157
4	-0.0100

Table 1.2: Lowest five eigenvalues of the unregulated Coulomb potential with the antisymmetric boundary condition ($\lambda = 1$, $\mu = 0.1$).

the domain of the operator $1/r^2$ by requiring $c_0 = 0$ in the basis state expansion $\sum_m c_m|m\mu\rangle$. A similar observation has been made previously in polymer quantization of a class of cosmological models, as a way to obtain singularity avoidance without recourse to the Thiemann trick [36, 37], and related discussion of the self-adjointness of polymer Hamiltonians arising in the cosmological context has been given in [38]. While we are not aware of a way to relate our system, with the $-1/r^2$ potential and no Hamiltonian constraints, directly to a specific cosmological model, it is nonetheless reassuring that the various techniques we have used in this case for dealing with the singularity all lead to quantitatively similar spectra.

Chapter 2

Dynamical Black Holes

2.1 Introduction

Black holes are one of the most interesting solutions to Einstein's field equations. They demonstrate in various ways the incompleteness of our classical understanding of gravity and provide hints toward developing a quantum theory. The relevant issues are the endpoint of Hawking radiation, the breakdown of general relativity at curvature singularities and the microscopic source of black hole entropy. Given the lack of experimental guidance, black holes provide a vital testing ground for new ideas in quantum gravity. Despite a great deal of analytic and numerical work, relatively little is known about the dynamics of black hole formation since the equations for collapsing matter fields tend to be very difficult to work with.

In this chapter we develop a mathematical model of black hole formation from the collapse of a massless scalar field in spherical symmetry. We use a system of coordinates developed independantly by Painlevé [8] and Gullstrand [9]. The key distinguishing feature of PG coordinates is that they are regular across apparent horizons where other coordinates tend

to be problematic. In principal, this allows for a representation of the entire spacetime without having to patch different coordinate systems together.

Black holes are usually described in terms of a singularity and an event horizon. However, a spacetime that begins with a singularity is not useful for describing black hole formation. Furthermore, event horizons are teleological; the entire spacetime must be known before these horizons can be located. Since the traditional framework is relevant only for eternal black holes and is incapable of descibing formation and evolution, a new paradigm in terms of trapping horizons is becoming increasingly popular for working with dynamical systems.

Within a given time slice, *apparent* horizons are locations where "outward" moving null geodesics are stationary. These horizons depend on the choice of spacetime slicings. They are dynamical; as mass within a system moves around, the apparent horizons may also move. This is in constrast to *event* horizons which are stationary, defined in the limit of time going to infinity (after all of the mass *that will ever* fall into the black hole has done so) as the point where outward moving null geodesics stand still. Take for example the (classical) Vaidya solution of dynamical black hole formation illustrated in Fig 2.1. An initial outer apparent horizon forms at some radius, moving outward until it coincides with the event horizon just as all of the mass has entered the black hole.

A two-dimensional trapping horizon in spacetime is mapped out by the path of the apparent horizons. We explore this new description of black holes by taking advantage of the PG coordinate system to run the code beyond initial horizon formation. We study the evolution of apparent horizons and generate spacetime diagrams and animations of dynamical black holes in terms of trapping horizons.

The system of equations we develop does not possess an analytical solution. To get past this hurdle, we have created a computer code which employs numerical methods to obtain solutions. Due to our choice of coordinates, we are able to simulate black hole formation

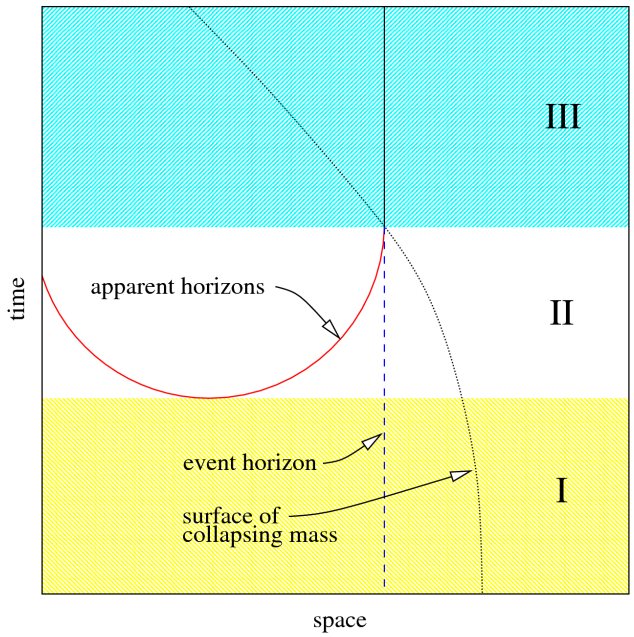

Figure 2.1: Spacetime diagram of the Vaidya solution of black hole formation illustrating the apparent horizons and event horizon. The spacetime is divided into three distinct regions: I) mass is collapsing inward, the density is insufficient for black hole formation; II) a black hole forms, the outer apparent horizon grows until it coincides with the event horizon just as the entire mass has fallen within, a singularity forms when the inner horizon reaches the origin; III) the black hole appears stationary to an exterior observer, though mass may continue moving around within the interior.

from initial scalar field data and watch the evolution of apparent horizons until the onset of singularity formation.

We first of all study the *critical behaviour* of the classical system. This topic has been studied in depth by a number of authors and provides several concrete tests for our code. All previous studies have used either Schwarzschild or null coordinates; ours is the first to use the PG system. We are able to accurately produce the expected results and also uncover some unexpected new behaviour resulting from our coordinate choice.

Having demonstrated that our code accurately produces the expected classical behaviour, we then add loop quantum gravity (LQG) motivated corrections which simulate the effects of

a discrete spacetime. Remarkably, we find the quantum system to exhibit two very important predictions of quantum gravity: singularity avoidance and a non-zero lower limit on black hole mass (a "mass gap").

2.2 Critical Behaviour

There are two possible outcomes for the gravitational collapse of an initial mass distribution: black hole formation or matter dispersion. Solutions that lead to black hole formation are called *supercritical*, while those that lead to matter dispersion and a flat spacetime are called *subcritical*. The critical solution in the zero mass limit terminates in finite proper time for a central observer.

The study of critical phenomena in gravitational collapse involves solutions in the near-critical regime. Pioneered by Choptuik [39] in the early 1990's, this topic has become an entire field of research and is a large subject in its own right (for an in-depth review see [40]). Here we consider only the properties that are relevant to this work.

The critical solution plays the role of an intermediate attractor in the phase space spanned by the parameters used to define the initial spacetime. For example, one parameter might correspond to the central location of the mass distribution while another could determine the initial momentum of the mass. The phase space dimension corresponds to the number of freely specifiable parameters, and each point corresponds to a spacetime. Within the phase space lies a critical solution hypersurface on which every point leads toward the intermediate attractor. Away from the critical surface, points on one side evolve toward black hole formation while points on the other side lead toward matter dispersion. Points very near the critical surface are initially attracted toward the critical solution, but are eventually repelled to either a black hole solution or the flat space fixed point. The closer a solution

is to criticallity, the more time it will spend near the intermediate attractor before being repelled. See Fig. 2.2 for an illustration.

In the case of massless scalar fields, the critical solution exhibits discrete self similarity (DSS) described in terms of a generic set of field variables by

$$Z_*(r,t) = Z_*(e^{m\Delta}r, e^{m\Delta}t), \tag{2.2.1}$$

where Z_* is the critical solution, r is the area radius, t is the time coordinate, $m \geq 0$ is an integer and Δ is a dimensionless real number. To explain this phenomena more clearly, consider the profiles of the critical solution field variables frozen in time at t_0. After a certain amount of time δt elapses, the same profiles will be found on a scale that is smaller by a factor of e^{Δ}. After an additional time $\delta t/e^{\Delta}$ has passed, the same profile will again be found on a scale that is $e^{2\Delta}$ times smaller than at t_0. This gives rise to the more descriptive name for DSS in gravitational collapse, scale echoing.

The existence of the intermediate attractor gives rise to scaling relationships for near critical solutions. For any one parameter family of data in the limit of small black holes one finds a mass scaling relation:

$$\ln(M_{BH}) \sim \gamma \ln|p - p_*| + f(\ln|p - p_*|), \tag{2.2.2}$$

where M_{BH} is the black hole mass on formation, γ is a real parameter referred to as the critical exponent, $f(\ln|p - p_*|)$ is a periodic function, p is any parameter in the initial data and p_* is the threshold value of that parameter that separates the data into supercritical and subcritical categories. Two separate analytical studies ([40], [41]) have shown that DSS

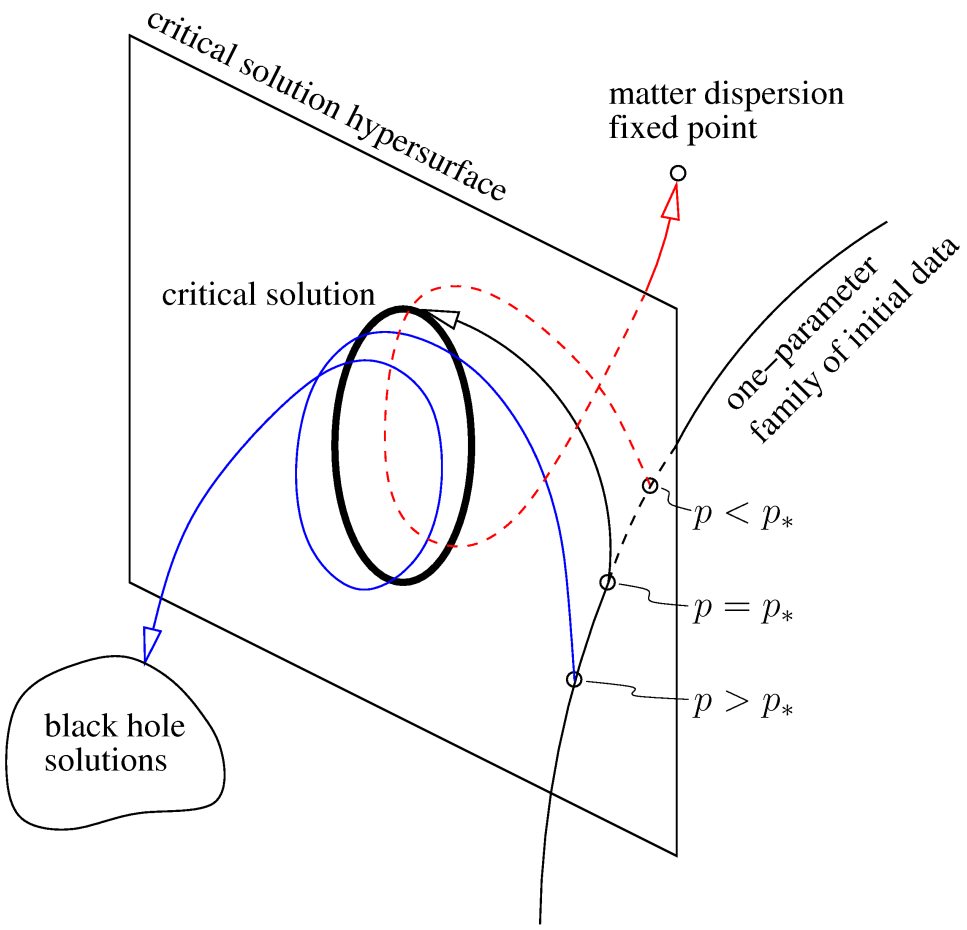

Figure 2.2: Phase space diagram of the collapse solutions. The wide ring in the centre of the critical hypersurface represents the limit cycle of the critical solution. The lines with arrows represent time evolutions of initial data. The line without arrows is a one-parameter (labeled p) family of initial data defined such that $p = p_*$ is the critical solution, $p > p_*$ is supercritical and $p < p_*$ is subcritical. Notice the time evolution of the critical solution (black line with arrow) evolves to the limit cycle. The supercritical initial point (blue line with arrow) is attracted to the limit cycle for some time before being repelled to a black hole solution, while the subcritical initial point (red line with arrow) is also attracted to the limit cycle but is repelled to the flat space fixed point. (Lines are dashed where they are behind the critical hypersurface from the illustration perspective.)

results in the period of $f(\ln|p-p_*|)$ being

$$T = \Delta/2\gamma. \tag{2.2.3}$$

Note that $f(\ln|p-p_*|)$ is often referred to as a "small oscillation" or "wiggle", but its explicit functional form must be determined numerically [40].

Garfinkle and Duncan have shown that a similar scaling relation exists for the maximum curvature in subcritical solutions [42]. For any one parameter family of data in the barely subcritical limit one finds:

$$\ln\left(\mathrm{MAX}_t\left\{R(r=0)\right\}\right) \sim -2\gamma\ln|p-p_*| + g(\ln|p-p_*|), \tag{2.2.4}$$

where $R(r=0)$ is the Ricci scalar at the origin and $g(\ln|p-p_*|)$ is a periodic component, again with period T. The notation MAX_t refers to the maximum found over all values of t. This relation is similar to that of mass scaling, except for the factor in front of $\ln|p-p_*|$ being -2γ rather than γ. This derives from mass having units of length whereas the Ricci scalar has units of $1/\mathrm{length}^2$.

The third aspect of critical collapse we note here is universality. DSS and critical scaling have been observed in the gravitational collapse of many different types of fields. The constants γ and Δ are determined by the properties of the critical solution and are therefore universal: they vary for different kinds of matter but are independent of the form of initial data and the parameter in that initial data that is varied. Numerical and semi-analytical calculations for the massless scalar field have given $\gamma \simeq 0.37$ and $\Delta \simeq 3.4$ [39, 40, 41, 43, 44, 45]. In previous calculations, all done in Schwarzschild or double null coordinates, the functions f and g were well approximated by a small amplitude sine function with period

$T = \Delta/2\gamma \simeq 4.6$.

2.3 Equations of Motion

The dynamical system that we wish to study is that of a collapsing spherically symmetric, massless scalar field in four spacetime dimensions. It turns out to be convenient to express these equations in a somewhat non-traditional parameterization, using the formalism of 2d dilaton gravity (see [46] for a general review of dilaton gravity and [47] for applications to black holes). In addition to providing a relatively simple form for the evolution equations in four dimensions, the formalism is generally applicable to a variety of spherically symmetric theories in four or more dimensions [45]. We will describe the formalism in some detail because the gauge fixing is a crucial part of our analysis. We begin by stating the classical action and defining a metric. We then perform a canonical transformation and fix the gauge to yield dynamical equations for the scalar field in PG coordinates.

We write the action for a massless scalar field ψ coupled to a dilaton field ϕ in 2d as

$$S[g, \phi, \psi] = S_G[g, \phi] + S_M[\psi, g, \phi], \tag{2.3.1}$$

where the gravity action is

$$S_G[g, \phi] = \frac{1}{2G} \int dx\, dt\, \sqrt{-g} \left(\phi R(g) + \frac{V(\phi)}{l^2} \right), \tag{2.3.2}$$

and the matter action is

$$S_M[\psi, g, \phi] = -\frac{1}{2} \int dx\, dt \sqrt{-g} h(\phi) |\nabla \psi|^2. \tag{2.3.3}$$

G is Newton's consant in 2d, g is the metric determinant, $R(g)$ is the Ricci scalar and $h(\phi)$ is the dilaton coupling.

The relationship of this action to spherically symmetric gravity in $D = n + 2$ dimensions is given as follows. The physical D metric is:

$$ds^2_{\text{phys}} = \frac{ds^2}{j(\phi)} + r^2(\phi) d\Omega_n^2, \tag{2.3.4}$$

where $d\Omega_n^2$ is the line element of the unit n-sphere and

$$j(\phi) := \int_0^\phi d\tilde{\phi} V(\tilde{\phi}). \tag{2.3.5}$$

With the further substitutions

$$\begin{aligned}
2G &= \frac{16\pi G^{(n+2)} n}{8(n-1)\nu^{(n)} l^n}, && (2.3.6)\\
\phi &= \frac{n}{8(n-1)} \left(\frac{r}{l}\right)^n, && (2.3.7)\\
V(\phi) &= (n-1) \left(\frac{n}{8(n-1)}\right)^{1/n} \phi^{-1/n}, && (2.3.8)\\
h(\phi) &= \frac{8(n-1)}{n} \phi = \left(\frac{r}{l}\right)^n, && (2.3.9)\\
\psi &= \sqrt{2\nu^{(n)} l^n} \widetilde{\psi}, && (2.3.10)
\end{aligned}$$

the dilaton action (2.3.1) is (up to boundary terms) precisely equal to that of a spherically symmetric massless scalar field $\widetilde{\psi}$ minimally coupled to Einstein gravity in D spacetime dimensions:

$$I^{(D)} = \frac{1}{16\pi G^{(D)}} \int d^D x \sqrt{-g^{(D)}} R^{(D)} - \frac{1}{2} \int d^D x \sqrt{-g^{(D)}} |\nabla \widetilde{\psi}|^2. \tag{2.3.11}$$

In the context of spherically symmetric gravity, performing the dimensional reduction in the action before varying yields the same dynamics as imposing spherical symmetry in the field equations themselves.

In order to make our coordinate choice explicit and rigorous, we present the Hamiltonian analysis for the theory. We use a metric in modified ADM (Arnowitt-Deser-Misner) form [48]:

$$ds^2 = e^{2\rho}\left(-\sigma^2 dt^2 + (dx + N dt)^2\right), \tag{2.3.12}$$

where ρ, σ and N are arbitrary functions of the spacetime coordinates. The lapse (σ) and shift (N) functions turn out to be Lagrange multipliers which give rise to constraints.

The two actions may be worked on separately to find the momenta. First, working with S_G to find Π_ϕ and Π_ρ, the Ricci scalar is found to be:

$$\begin{aligned} R &= -\frac{2}{\sigma^3}e^{-2\rho}\Big(\sigma\rho'\dot{N} - \dot{\sigma}N\rho' - \dot{\sigma}N' + \dot{\sigma}\dot{\rho} + \sigma\dot{\rho}N' + \sigma^2\rho'\sigma' - 2\sigma N\rho'N' \\ &\qquad -\sigma' N r\dot{h}o + \sigma' N^2\rho' + \sigma' N N' + 2\sigma N\dot{\rho}' + \sigma\dot{N}' \\ &\qquad -\sigma\ddot{\rho} + \sigma^3\rho'' + \sigma^2\sigma'' - \sigma N^2\rho'' - \sigma(N')^2 - \sigma N N''\Big), \end{aligned} \tag{2.3.13}$$

where the primes denote differentiation with respect to x, and the dots signify time differentials. We substitute this into (2.3.2) and use integration by parts to work out the Lagrangian. Ignoring surface terms, we find

$$\begin{aligned} L_G &= \frac{1}{2G}\int dx\Big[\frac{V\sigma e^{2\rho}}{l^2} + \frac{2}{\sigma}\Big(\dot{\phi}\rho' N + \phi' N\dot{\rho} + \dot{\phi}N' - \dot{\phi}\dot{\rho} \\ &\qquad -\phi' N^2\rho' - \phi' N N' + \sigma^2\phi'\rho' - \sigma\sigma''\phi\Big)\Big]. \end{aligned} \tag{2.3.14}$$

Taking the necessary functional derivatives of L_G, we find the momenta:

$$\Pi_\phi = \frac{1}{\sigma G}\left(\rho' N + N' - \dot{\rho}\right), \tag{2.3.15}$$

$$\Pi_\rho = \frac{1}{\sigma G}\left(\phi' N - \dot{\phi}\right). \tag{2.3.16}$$

Now, we must work on the matter action to find Π_ψ. Working from (2.3.3), we find the matter Lagrangian to be

$$L_M = -\frac{1}{2}\int dx \;\; \sigma e^{2\rho} h(\phi)\left(g^{tt}(\dot{\psi})^2 + 2g^{tx}\dot{\psi}\psi' + g^{xx}(\psi')^2\right). \tag{2.3.17}$$

Taking the functional derivative with respect to $\dot{\psi}$, we find

$$\Pi_\psi = \frac{h(\phi)}{\sigma}(\dot{\psi} - N\psi'). \tag{2.3.18}$$

Substituting momenta for velocities, it is now possible to form the Hamiltonian in terms of conjugate momenta and positions. We find

$$H = \int dx\, (\sigma\mathcal{G} + N\mathcal{F}) + H_B, \tag{2.3.19}$$

where H_B are the boundary terms that are required to make the variational principal well defined. These will not have any affect on the equations of motion and can be fixed to satisfy boundary conditions. $\mathcal{G}$ is the Hamiltonian constraint:

$$\mathcal{G} = \frac{\phi'' - \phi'\rho'}{G} - G\Pi_\phi\Pi_\rho - \frac{e^{2\rho}}{2G}\frac{V(\phi)}{l^2} + \mathcal{G}_M, \tag{2.3.20}$$

where

$$\mathcal{G}_M = \frac{1}{2}\left(\frac{\Pi_\psi^2}{h(\phi)} + h(\phi)(\psi')^2\right) \tag{2.3.21}$$

is the energy density of the scalar field. The Hamiltonian constraint will give us the physical laws of the system. The *diffeomorphism* constraint $\mathcal{F}$ puts a requirement on the phase space variables given by:

$$\mathcal{F} = \rho'\Pi_\rho - \Pi_\rho' + \phi'\Pi_\phi + \psi'\Pi_\psi. \tag{2.3.22}$$

$\mathcal{G}$ and $\mathcal{F}$ are primary constraints, and are first class with each other (they have a Poisson bracket equal to zero).

For future reference, note that the linear combination,

$$\begin{aligned}\widetilde{\mathcal{G}} &:= le^{-2\rho}\phi'\mathcal{G} + lGe^{-2\rho}\Pi_\rho\mathcal{F} \\ &= -\mathcal{M}' + \frac{l}{2}e^{-2\rho}\phi'\left(\frac{\Pi_\psi^2}{h(\phi)} + h(\phi)(\psi')^2 + \frac{2G\Pi_\rho\Pi_\psi\psi'}{\phi'}\right),\end{aligned} \tag{2.3.23}$$

yields a new Hamiltonian constraint in terms of the mass function,

$$\mathcal{M} = \frac{l}{2G}\left(e^{-2\rho}\left[(G\Pi_\rho)^2 - (\phi')^2\right] + \frac{j(\phi)}{l^2}\right). \tag{2.3.24}$$

$\mathcal{M}$ is called the mass function because it approaches a constant at spatial infinity where it is equal to the ADM mass of the solution.

The next step is to fix the gauge freedom with appropriate conditions. The first gauge choice is

$$\chi = j(\phi) - l\phi' \approx 0, \tag{2.3.25}$$

where we use ≈ 0 to mean weakly equal to zero (using constraints after all Poisson brackets have been found).

It is necessary for a gauge choice to be second class with at least one of the primary constraints. Using smearing functions $a(x)$, $b(x)$ which vanish on the boundary, we find

$$\{\chi(a), \mathcal{F}(b)\} = \int dx\; bj(\phi) \left(a' + \frac{dj(\phi)}{d\phi} a \right), \tag{2.3.26}$$

which is non-zero, defining χ to be second class with $\mathcal{F}$. Using the formalism of Dirac brackets, we are able to set second class constraints strongly equal to zero and use these to reduce the Hamiltonian. Taking χ as a strong identity removes ϕ and Π_ϕ from the dynamics, and implies that our spatial coordinate is the radius of invariant two spheres. Because the remaining phase space variables (ρ, Π_ρ, ψ, Π_ψ) all commute with χ, the Dirac brackets for these variables are the same as the Poisson brackets, and we can continue working with the more simple Poisson brackets.

Requiring this gauge fix to be preserved in time, i.e.

$$\dot{\chi} = \{\chi, H\} = 0, \tag{2.3.27}$$

yields a consistency condition on the lapse and shift functions,

$$\sigma G \Pi_\rho = N \phi', \tag{2.3.28}$$

which we will use to substitute for N in favour of σ.

The equations are put in a more transparent form using the canonical transformation:

$$X := e^{\rho}, \tag{2.3.29}$$

$$P := e^{-\rho} G \Pi_\rho. \tag{2.3.30}$$

P is then conjugate to X with their Poisson bracket being

$$\{X(x), P(y)\} = G\delta(x, y). \tag{2.3.31}$$

Choosing the boundary term to make the variational principal well defined at the boundary, we find the resulting Hamiltonian to be

$$H(X, P, \psi, \Pi_\psi) = \int dr\ \sigma\mathcal{C} + \int dr \left(\frac{\sigma X^2}{j(\phi)}\mathcal{M}\right)' \tag{2.3.32}$$

where

$$\mathcal{C} = \left(-\frac{X^2}{j(\phi)}\mathcal{M}' + \mathcal{G}_\mathcal{M} + l\frac{XP\psi'\Pi_\psi}{j(\phi)}\right), \tag{2.3.33}$$

$$\mathcal{M} = \frac{l}{2G}\left(P^2 - \frac{(\phi')^2}{X^2} + \frac{j(\phi)}{l^2}\right), \tag{2.3.34}$$

$$\mathcal{G}_\mathcal{M} = \frac{1}{2}\left(\frac{\Pi_\psi^2}{h(\phi)} + h(\phi)(\psi')^2\right). \tag{2.3.35}$$

We now completely fix the gauge by choosing

$$\zeta = X - \sqrt{j(\phi)} \approx 0. \tag{2.3.36}$$

This condition is second class with the remaining constraint $\mathcal{C}$, as evident by the non-zero Poisson bracket:

$$\{\zeta(a), \mathcal{C}(b)\} = \int dx\ 2la\left(\frac{b'}{G}XP + b\psi'\Pi_\psi\right). \tag{2.3.37}$$

Similarly to our first gauge choice, we may therefore use ζ as a strong identity to further reduce the Hamiltonian, so long as we use Dirac brackets in finding the equations of motion. X and P become purely kinematical, and the remaining phase space variables (ψ and Π_ψ)

commute with ζ so that the Dirac brackets are equivalent to the Poisson brackets.

Notice that (2.3.36) along with (2.3.34) and (2.3.25) imply

$$P^2 = \frac{2G}{l}\mathcal{M}. \tag{2.3.38}$$

We will subsequently use $\mathcal{M}$ rather than P in our equations since it is more familiar in black hole physics.

The gauge used here produces the non-static generalization of PG coordinates, as can be seen by using (2.3.28) and the gauge conditions to reduce the line element to the spatially flat form [50]:

$$ds^2 = j(\phi)\left[-\sigma^2 dt^2 + \left(dr + \sqrt{\frac{2G\mathcal{M}l}{j(\phi)}}\sigma dt\right)^2\right]. \tag{2.3.39}$$

More importantly, the spatial slices will be seen to be regular across apparent horizons that form during the evolution.

We are now able to write the equations of motion for the scalar field in fully reduced form:

$$\dot{\psi} = \sigma\left(\frac{l\sqrt{2G\mathcal{M}/l}\psi'}{\sqrt{j(\phi)}} + \frac{\Pi_\psi}{h(\phi)}\right), \tag{2.3.40}$$

$$\dot{\Pi}_\psi = \left[\sigma\left(h(\phi)\psi' + \frac{l\sqrt{2G\mathcal{M}/l}\Pi_\psi}{\sqrt{j(\phi)}}\right)\right]', \tag{2.3.41}$$

where $\mathcal{M}$ and σ are the solutions to

$$\mathcal{M}' = \mathcal{G}_\mathcal{M} + l\psi'\Pi_\psi\sqrt{\frac{2G\mathcal{M}l}{j(\phi)}}, \tag{2.3.42}$$

$$\sigma' = -\frac{Gl\psi'\Pi_\psi\sigma}{\sqrt{2G\mathcal{M}lj(\phi)}}. \tag{2.3.43}$$

The right hand side of (2.3.42) defines the instantaneous mass density of the configuration. It has the expected contribution from the energy density of the scalar and an additional coupling term that corresponds to the contribution from its self gravity. Note that these equations are invariant under the rescaling:

$$t \to kt, \qquad r \to kr, \qquad l \to kl, \qquad \psi \to \psi, \qquad \Pi_\psi \to k^{-1}\Pi_\psi, \tag{2.3.44}$$

meaning that no intrinsic scale exists classically.

The above equations need to be supplemented by boundary conditions for $\mathcal{M}$ and σ. Without loss of generality we choose $\sigma(t, r = 0) = 1$. A change in this value corresponds to a trivial rescaling of the time coordinate. We also fix $\mathcal{M}(t, r = 0) = 0$, which guarantees that the metric is flat in the neighbourhood of the origin. In fact, a non-zero value of $\mathcal{M}$ at the origin signals the formation of a singularity, so that this boundary condition would have to be relaxed/modified in order to integrate the equations past singularity formation.

In this paper we work exclusively in four dimensions, so we have $n = 2$. This sets

$$\phi = r^2/(4l^2); \tag{2.3.45}$$

$$j(\phi) = \sqrt{\phi} = r/2l; \tag{2.3.46}$$

$$h(\phi) = 4\phi = r^2/l^2. \tag{2.3.47}$$

For convenience we choose $2G = 1$, which from Eq.(2.3.6) corresponds to choosing the characteristic length scale l to be $l_{pl} = \sqrt{G^{(4)}}$.

2.4 Computational Methods

Computational methods[1] are used to solve the equations of motion. The framework of these calculations will consist of a grid of the spacetime coordinates. The integration methods we employ will need only enough memory for a single time slice. Arrays are used to represent the r-lattice and the values of the fields at each time slice. The fields are calculated anew after each time step, while the r-lattice remains fixed throughout the evolution.

The most interesting behaviour occurs as matter approaches the origin on ever finer scales. In order to observe this small r behaviour while keeping a large enough lattice to contain all of the mass within the system (numerical errors occur when mass leaves the grid), we refine the r-spacing $\Delta r(r)$ near the origin so that it is several orders of magnitude smaller than the spacing near the outer endpoint. We define the first point $r_0 = 0$ and step away in small increments for some distance, covering the region of interest with a finely spaced lattice. The step size then gradually increases until it reaches some maximum coarse size capable of handling the dynamics. The endpoint extends far enough to maintain all of the mass within the system. The lattice remains fixed throughout the evolution.

After defining the r-lattice, we specify initial ψ and Π_ψ configurations. We work with two forms:

$$\psi = Ar^2 \exp\left[-\left(\frac{r-r_0}{B}\right)^2\right], \tag{2.4.1}$$

$$\psi = A \tanh\left(\frac{r-r_0}{B}\right), \tag{2.4.2}$$

where A, B and r_0 are the parameters which may be varied to study critical collapse. We shall refer to these two forms of initial data as gaussian and tanh respectively. For both

[1]The code was written in c++.

cases we define an initial standing wave by choosing $\Pi_\psi(r,0) = 0$. Note that since the initial mass density depends on ψ', the tanh form has one mass peak while the gaussian data has two.

We use an adaptive time step $\Delta t(t)$ refinement according to the minimum found across the spacial slice using the condition

$$\Delta t(t) = \mathrm{MIN}_r \left\{ \frac{dt}{dr} \Delta r(r) \right\}, \tag{2.4.3}$$

where $\frac{dt}{dr}$ is the inverse of the local speed of an ingoing null geodesic. This provides stability by preventing information from moving over too many r-points in a single time step. Having Δt proportional to Δr greatly increases computational times for finer r-spacing, placing a practical lower limit on the size of black holes that we are able to create. However, this is not a significant concern as we are able to work on small enough scales to produce critical mass scaling.

Both time and space integrations are performed using Runge-Kutta methods accurate to fourth order in the local grid spacing. To step forward with respect to some variable z, we need the fields $\vec{y}$ defined at some initial z_0. We denote the total derivatives of the fields

$$f_i(z, \vec{y}) := \frac{dy_i}{dz}. \tag{2.4.4}$$

A step forward Δz is taken using

$$y_i(z + \Delta z) = y_i(z) + \frac{\Delta z}{6} \left[A_i(z) + 2B_i(z) + 2C_i(z) + D_i(z) \right] + \mathbb{O}\left(\Delta z^5\right), \tag{2.4.5}$$

where

$$A_i(z) = f_i\left(z, \vec{y}\right); \tag{2.4.6}$$

$$B_i(z) = f_i\left(z + \frac{\Delta z}{2}, \vec{y} + \frac{\Delta z}{2}\vec{A}(z)\right); \tag{2.4.7}$$

$$C_i(z) = f_i\left(z + \frac{\Delta z}{2}, \vec{y} + \frac{\Delta z}{2}\vec{B}(z)\right); \tag{2.4.8}$$

$$D_i(z) = f_i\left(z + \Delta z, \vec{y} + \Delta z\vec{C}(z)\right). \tag{2.4.9}$$

Note that Δz may be different at each step, as is the case in our code.

We use three-point[2] central finite differences[3] to calculate the spatial derivatives, switching to forward differences at the origin and backward differences at the outer end point. With three points, the accuracy is up to second order in the local spacing, although it is third order where the spacing is uniform due to a cancellation in the second order term. The first order derivative is given by

$$\begin{aligned}\left(\frac{\partial y}{\partial z}\right)_j = &-\left(\frac{h_i + h_{i+1}}{-h_i h_{i-1} + h_i h_{i+1} + h_{i-1}h_{i-1} - h_{i+1}h_{i-1}}\right) y_{i-1} \\ &+\left(\frac{h_{i-1} + h_{i+1}}{-h_{i+1}h_{i-1} + h_i h_{i-1} - h_i h_i + h_i h_{i+1}}\right) y_i \\ &-\left(\frac{h_{i-1} + h_i}{-h_{i+1}h_{i-1} + h_i h_{i-1} + h_{i+1}h_{i+1} - h_i h_{i+1}}\right) y_{i+1},\end{aligned} \tag{2.4.10}$$

[2]Since our lattice spacing tends to increase when moving away from the origin, information used from points on the right side can be from further away than information collected from points on the left. Trying to increase the finite difference accuracy by using data from more points is unsuccessful since the problem of lopsidedness worsens, making the code unstable.

[3]We also experimented with cubic splines finding the same qualitative behaviour as for finite differences, which gives some indication of reliability. In the end we chose to use finite differences exclusively since they require less computational time.

and the second order derivative by

$$\begin{aligned}\left(\frac{\partial^2 y}{\partial z^2}\right)_j = &\left(\frac{2}{-h_i h_{i-1} + h_i h_{i+1} + h_{i-1} h_{i-1} - h_{i+1} h_{i-1}}\right) y_{i-1} \\ &- \left(\frac{2}{(-h_{i+1} h_{i-1} + h_i h_{i-1} - h_i h_i + h_i h_{i+1}}\right) y_i \\ &+ \left(\frac{2}{-h_{i+1} h_{i-1} + h_i h_{i-1} + h_{i+1} h_{i+1} - h_i h_{i+1}}\right) y_{i+1}.\end{aligned} \tag{2.4.11}$$

Here, the lattice points are labelled by i. The notation is capable of describing forward, backward and central differences. We set $j = i$ everywhere, except at the inner and outer endpoints where $j = i - 1, i + 1$ respectively. The lattice spacings are labelled such that $h_i = r_i - r_j$.

In studying the critical behaviour, critical parameters were found to an accuracy of $\partial p/p \sim 10^{-15}$ using a binary search. We tried a variety of grid resolutions with r-spacings[4] near the origin ranging from 10^{-6} to 10^{-3}, which in turn affects the t-spacings. Convergence of our code is apparent since the results were not affected by increasing the resolution beyond 10^{-3} as long as the black hole size on formation was sufficiently large enough compared to the grid size. Thus further decreases in grid size merely allowed us to continue the runs closer to criticality. To ensure the stability of our code, we monitor the ADM mass for each run and find it to remain constant within $\sim 0.03\%$.

[4]Since the system is scale invariant, we introduce r_0 as a measure and give values for the resolution in terms of $\Delta(r)/r_0$.

The following is a basic overview of the code:

a. define r_i and $\Delta r(r)$;

b. define initial ψ and Π_ψ on r_i;

c. begin loop (

   i. find ψ', ψ'' and Π'_ψ using finite differences;

   ii. solve for $\mathcal{M}$ and σ across r_i using Runge-Kutta methods;

   iii. calculate and output items of interest;

   iv. determine the size of the next time step using (2.4.3);

   v. integrate $\dot{\psi}$ and $\dot{\Pi}_\psi$ forward in time with Runge-Kutta methods;

d.) end loop.

2.5 Quantum Corrections

This model presents an excellent venue for observing the effects of quantum gravity on black hole formation and evolution. A general consensus among theories of quantum gravity is that spacetime should be discrete. In this section we introduce a quantum length scale to simulate a discrete space time and use this factor in modifying the classical equations of motion.

Since a quantum theory must preclude divergences, we look to modify terms deriving from the potential which may become infinite at the origin. Recall that $j(\phi(r)) = r/2l$ is defined as the integral of the potential. Looking at (2.3.40–2.3.43), we see that each equation has a divergent term with a $\sqrt{j(\phi)}$ in the denominator. Note that the coupling $h(\phi(r)) = r^2$

is also found in some denominators, but these terms are kinematical and in fact do not diverge.

Recall from Chapter 1 that it is necessary to extend the positive semidefinite r coordinate across the real line to $x \in \mathbb{R} \setminus \{0\}$ in order to use central finite differences as in (1.3.21). Using a slightly different notation here, we write

$$\frac{\mathrm{sgn}(x)}{\sqrt{|x|}} = 2\frac{d(\sqrt{|x|})}{dx} = \frac{\sqrt{|x+\mu|} - \sqrt{|x-\mu|}}{\mu} + \mathbb{O}(\mu^2), \tag{2.5.1}$$

where μ is the quantum length scale. This may be generalized to a variable lattice spacing $\mu(r)$ which yields a more complicated form with the same qualitative properties. It is important to remember that this correction may be derived from LQG principles.

Now, consider a function that diverges at $x = 0$ similarily to the terms we wish to modify in the equations of motion:

$$f_{unreg}(x) = \frac{1}{|x|}. \tag{2.5.2}$$

We obtain a regulated version of this function by squaring the right hand side of (2.5.1) and dropping the $\mathbb{O}(\mu^2)$ terms:

$$f_{reg}(x) = \left(\frac{\sqrt{|x+\mu|} - \sqrt{|x-\mu|}}{\mu} \right)^2. \tag{2.5.3}$$

This regulated version has a cusp at $x = \mu$ where the derivative w.r.t. x is discontinuous. As in [51], we instead use a smoothed function that has the same qualitative features as f_{reg}: it is nearly equal to f_{unreg} for $x \gg \mu$, it has a maximum at $x = \mu$ and it is equal to zero at $x = 0$.

$$f_{smooth}(x) = \frac{1}{|x|}\left[1 - e^{-\left(\frac{x}{\mu}\right)^2}\right]. \tag{2.5.4}$$

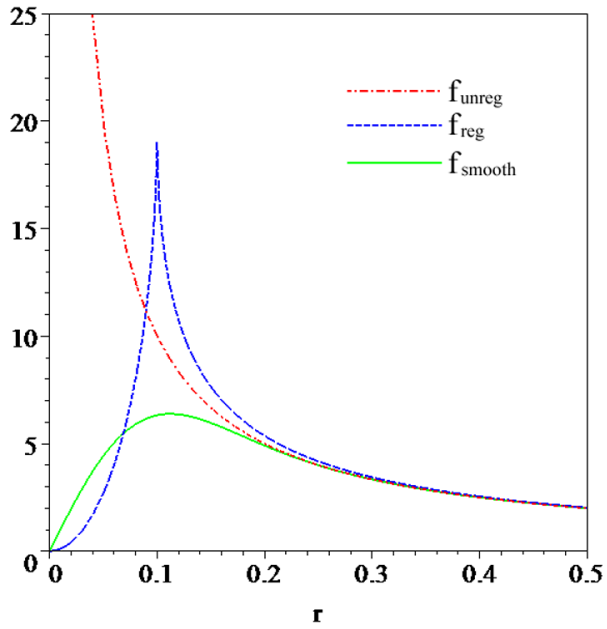

Figure 2.3: A comparison of $f_{unreg}(r)$, $f_{reg}(r)$ and f_{smooth}(r).

Since the equations of motion depend on $r \geq 0$ (rather than x) we revert to the radial coordinate. See Fig. 2.3 for a comparison of f_{unreg}, f_{reg} and f_{smooth} in this domain. The quantum correction to the equations of motion is the replacement

$$\frac{1}{\sqrt{j(r)}} \to \sqrt{2lf_{smooth}(r)}. \tag{2.5.5}$$

in each of (2.3.40–2.3.43).

These corrections effectively add a repulsive component to the gravitational potential very near the origin. This is consistent with the LQG prediction that the underlying discreteness at the quantum level will give rise to a short range repulsion in the semiclassical limit. Note that μ also introduces a length measure into this classically scale-invariant system.

2.6 Results

2.6.1 Classical Black Holes

Since our coordinates are regular across apparent horizons, we are able to evolve well beyond initial black hole formation up to the point when a singularity begins to form and our boundary conditions at the origin are no longer valid. The spacetime diagrams of classical black hole formation and evolution in Fig. 2.4 provide a neat description of dynamical black holes in terms of trapping horizons. A more dramatic illustration is given by the animations available for viewing at *http://theoryx5.uwinnipeg.ca/users/jziprick/*. These movies correspond to the spacetime maps in Fig. 2.4, showing the mass density profile and location of apparent horizons (vertical red lines) during black hole formation. Note that while the animations of classical collapse show a negative mass density in some regions just prior to singularity formation, the ADM mass at infinity remains constant.

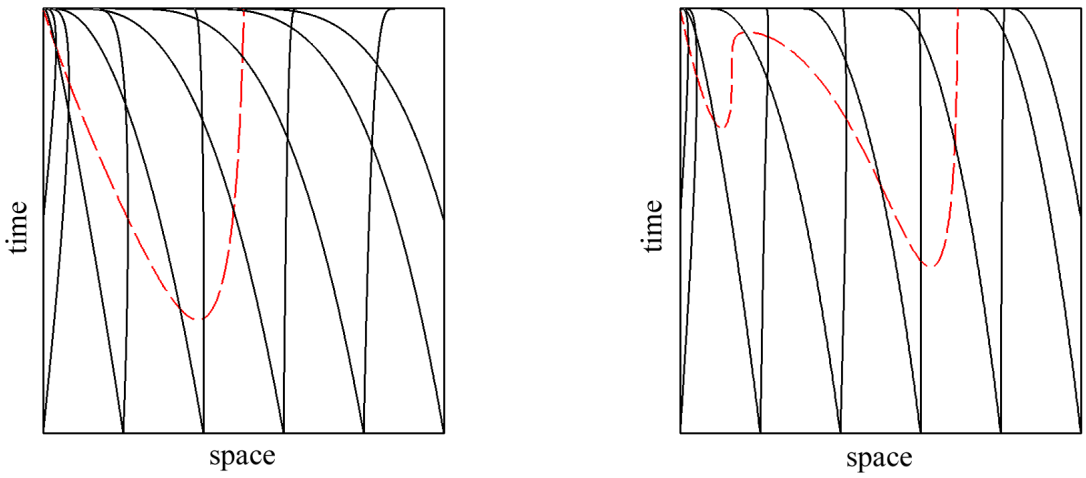

(a) tanh initial data (b) gaussian initial data

Figure 2.4: Diagrams of the classical spacetime for the collapsing massless scalar field using radius for the space axis and PG time for the time axis. The solid black lines are null geodesics and the dashed red lines indicate the trapping surface boundary.

We note that apparent horizons form in pairs within constant PG time slices. This is to be expected from looking at the function

$$AH = |\Delta\phi|^2 \tag{2.6.1}$$

$$= r - 2G\mathcal{M}, \tag{2.6.2}$$

which is equal to zero at apparent horizons. Initially AH is positive across the r-axis; minima begin to form as mass collapses inward. Black hole formation is signalled by the appearance of a single horizon (r_h) where the function first dips to zero. This horizon splits into two as the minimum drops below zero; the outer horizon (r_{oh}) continues to grow as mass passes through it while the inner horizon moves toward the origin. The singularity forms when the inner horizon reaches the origin, at which point the code terminates. The outer horizon remains stationary once it has reached its maximum radius; it cannot decrease because the scalar field obeys the standard energy conditions. Depending upon the initial mass distribution, subsequent horizon pairs may form as shown in Fig. 2.4(b) which depicts the evolution of gaussian initial data. The horizon paths define a two dimensional trapping surface in spacetime within which all null geodesics point toward the origin, as expected in theory [52].

In our study of the critical behaviour, we varied the parameters A, B, and r_0 in the gaussian form of initial data, and A in the tanh form. The critical values were found to an accuracy of $\partial p/p \sim 10^{-15}$ using a binary search. We tried a variety of grid resolutions with r-spacings near the origin ranging from 10^{-6} to 10^{-2}, which in turn affects the t-spacings. The accuracy was roughly equal in all cases where black hole size was not significantly affected by the resolution (when $r_h \gg \Delta r(r_h)$). However, finer grids allowed for data to be found for lower values of $\ln(p - p_*)$ thus showing critical scaling over a wider range of a given

parameter.

To demonstrate scale echoing, we present a plot of the scalar field at $r = 0$ as a function of $\tau = \ln(t_* - t)$ for the nearest solution to criticality that was numerically achieved using an r-spacing near the origin of 10^{-5}. t_* is the time of black hole formation in the critical solution given by the value approached asymptotically in the small mass limit. Since we set $\sigma(t, r = 0) = 1$ as a boundary condition, t is equivalent to the proper time at the origin. $\psi(\tau, r = 0)$ is seen to be periodic in τ with a period of $\Delta = 3.43 \pm 0.06$ found by averaging over the two oscillations between the minima at $\tau \sim -2.5$ and -9.3, with an error determined by the uncertainty in t_*. This result is in good agreement with the accepted value of $\Delta \simeq 3.44$.

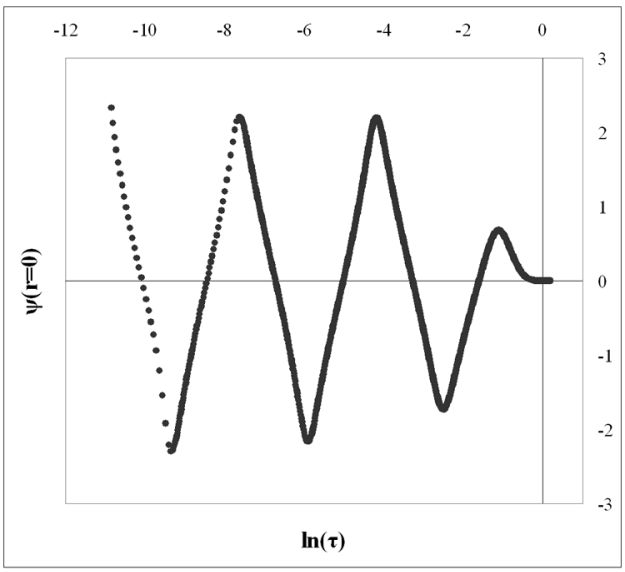

Figure 2.5: A plot of the scalar field at the origin versus τ illustrating scale echoing in the critical classical solution. The r-spacing used in generating this data was 10^{-5} near the origin.

Table 2.1 lists the critical exponent and period found for various lattice resolutions and families of initial data using both the mass and maximum curvature scaling relations. Our results in all cases are seen to agree with the accepted values of $\gamma \simeq 0.374$ and $T \simeq 4.6$.

type of scaling	form of initial data	parameter varied	resolution near origin	γ	T
curvature	gaussian	A	10^{-5}	0.376 ± 0.004	4.60 ± 0.02
curvature	gaussian	A	10^{-4}	0.377 ± 0.006	4.63 ± 0.05
mass	gaussian	A	10^{-5}	0.375 ± 0.004	4.6 ± 0.1
mass	gaussian	A	10^{-4}	0.374 ± 0.004	4.4 ± 0.2
mass	gaussian	B	10^{-4}	0.376 ± 0.006	4.4 ± 0.2
mass	gaussian	r_0	10^{-4}	0.377 ± 0.005	4.4 ± 0.2
mass	tanh	A	10^{-4}	0.371 ± 0.004	4.5 ± 0.1

Table 2.1: The critical exponent and period of the classical mass scaling curve for various initial data and mesh resolutions.

In studying the maximum subcritical curvature scaling behaviour classically, we determine the Ricci scalar R from the stress-energy tensor using the Einstein field equations. The stress-energy tensor is defined as

$$T_{\mu\nu} = \nabla_\mu \widetilde{\psi} \nabla_\nu \widetilde{\psi} - \frac{1}{2} g_{\mu\nu} \left| \nabla \widetilde{\psi} \right|^2, \tag{2.6.3}$$

where $\widetilde{\psi}$ is the 4D scalar field. With the field equations,

$$R_{\mu\nu} - \frac{1}{2} g_{\mu\nu} R = 8\pi G^{(4)} T_{\mu\nu}, \tag{2.6.4}$$

we determine the Ricci scalar in terms of the 2D scalar field variables:

$$\begin{aligned} R &= -g^{tt}\dot{\psi}^2 + 2g^{tr}\dot{\psi}\psi' - g^{rr}(\psi')^2 && (2.6.5) \\ &= \frac{l^4 \Pi^2}{r^4} - (\psi')^2. && (2.6.6) \end{aligned}$$

This form is simple to work with and allows for fast computation.

A plot of the maximum subcritical curvature scaling behaviour is given in figure 2.6(a).

γ was determined using a least squares linear fit over the points where the solution is seen to follow the intermediate attractor. The error quoted indicates how this value changes depending on the range of points chosen[5]. Figure 2.6(b) shows the residual left after subtracting the linear fit from the data. The period and associated error (at 95% confidence) were determined by fitting a sinusoidal function to the residual.

Next we look at the supercritcal mass scaling behaviour. In Fig. 2.7 we present the data found using a grid spacing of $\Delta r/r_0 = 10^{-4}$ near the origin. Comparing this with Fig. 2.8 found with $\Delta r/r_0 = 10^{-5}$ near the origin, one sees that the critical behaviour is followed over more periods with the finer grid since the solutions are able to exhibit Choptuik scaling down to lower values of $\ln|p - p_*|$.

On each of these supercritical plots we have drawn a line that osculates the peaks of the curves. The values of γ were determined using a least squares linear fit through the data points that are very near this line (within $\sim$ 5 % of M_{BH}). The error quoted represents the variance depending upon the choice of points. The periods are found by averaging the distance between the cusp-like valleys, with the error representing the uncertainty in locating the cusps. The data used in these calcultions consisted of the two periods corresponding to the lowest range of the parameter that produced black holes such that the size was not significantly affected by lattice resolution (for example, the periods between $\ln|A - A_*| \sim -9$ and -18 in figure 2.8 were used to calculate the values given in the third row of table 2.1).

Previous studies of critical collapse (done in either Schwarzschild or null coordinates) have shown both scaling relationships to be a slight oscillation about a straight line that is well approximated by a sine function. While this is confirmed by our results for the

[5]Note that the standard deviation of the slope given by the linear fit is not used for the error since the data is known to oscillate. The standard deviation would be non-zero even with "perfect" data. However, the error as found by comparing values when choosing different points turns out to be the same order of magnitude as the standard deviation.

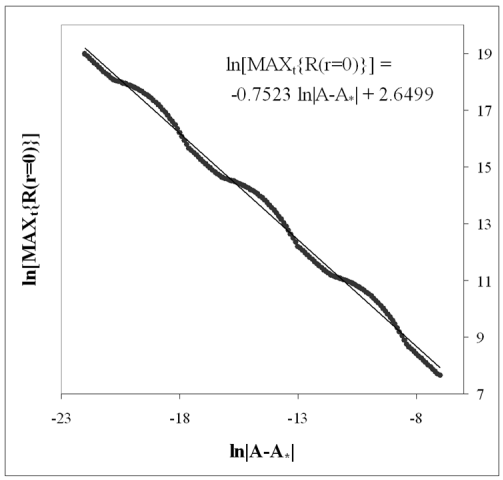

(a) Curvature scaling with linear fit.

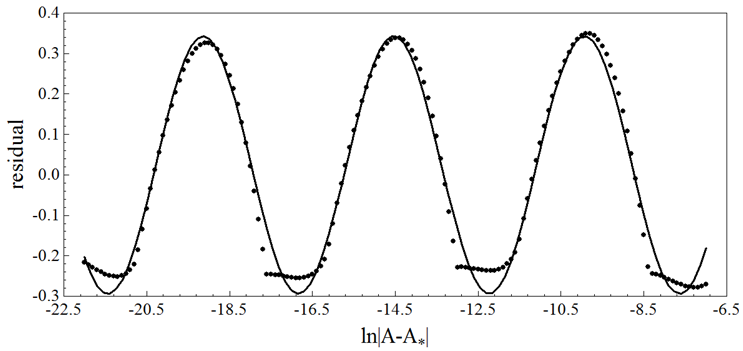

(b) Residual plot with sinusoidal fit. The flat bottoms of the periodic component were also observed in [42] and [56].

Figure 2.6: The subcritical maximum curvature scaling relation using the classical equations. The parameter A in gaussian initial data is varied, and $\Delta r/r_0 = 10^{-5}$ near the origin. The residual is found by subtracting the data in Fig. 2.6(a) from the linear fit.

(coordinate invariant) subcritical maximum curvature scaling, it is clearly not the case for our (coordinate dependant) supercritical mass scaling results where we find a periodic form with relatively large amplitude and a distinctly different functional form. Considering that our results agree with the known parameters of Choptuik scaling for varied initial data and mesh resolutions, and that our new-found periodic form is universal within the class of coordinate systems that we are using, it is unlikely that this periodic form is a numerical

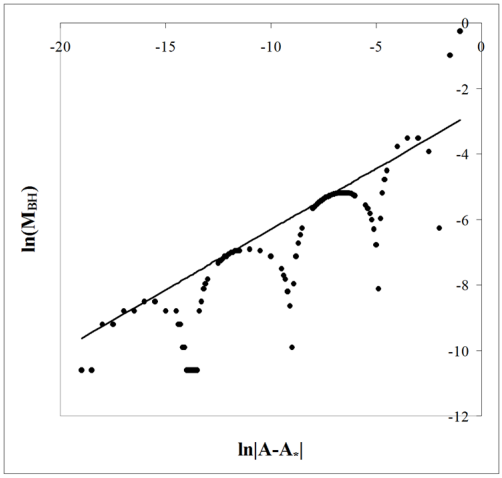

(a) Variation of the parameter A in gaussian initial data.

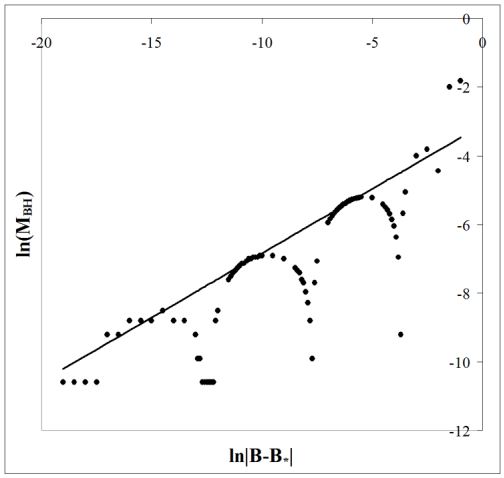

(b) Variation of the parameter B in gaussian initial data.

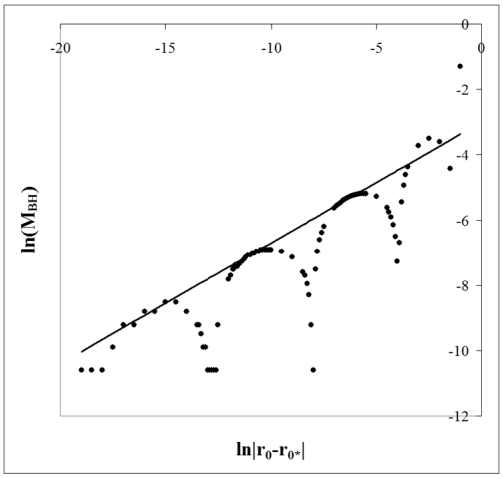

(c) Variation of the parameter r_0 in gaussian initial data.

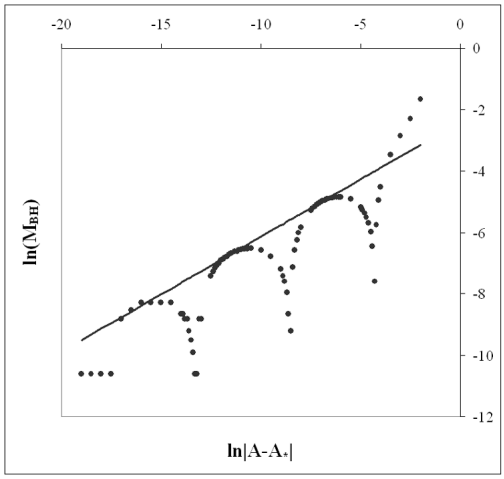

(d) Variation of the parameter A in tanh initial data.

Figure 2.7: Plots of the classical mass scaling behaviour with $\Delta r/r_0 = 10^{-4}$ near the origin.

artifact.

2.6.2 Quantum Black Holes

Having examined classical black hole formation and evolution, it was of great interest to look at this process using the quantum corrected equations of motion. Remarkably, the spacetime

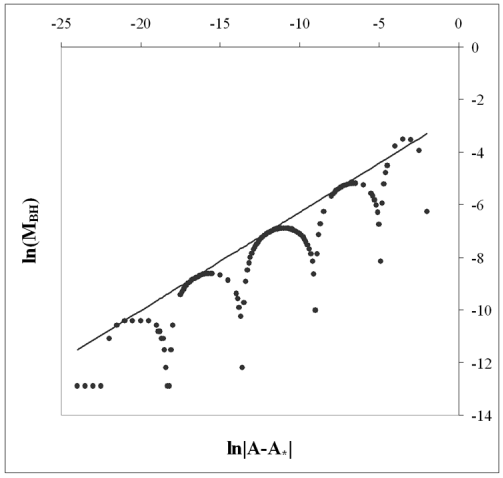

Figure 2.8: A plot of the supercritical mass scaling behaviour using the classical equations. The parameter A was varied in gaussian initial data with $\Delta r/r_0 = 10^{-5}$ near the origin.

diagrams modelling quantum black holes in Fig. 2.9 clearly illustrate singularity avoidance. Animations[6] of the mass density time evolution corresponding to Fig. 2.9 are available at *http://theoryx5.uwinnipeg.ca/users/jziprick/* .

In both cases inner and outer apparent horizons appear at some initial PG time and then separate as the inner horizon moves inward. Between the two horizons exist trapped surfaces on which all null rays move inward. As the inner horizon nears the quantum length scale it begins to slow down, eventually bouncing and moving outward without ever reaching the origin. Near the bounce, the mass density takes on negative values. This leads to mass loss and causes the outer horizon to shrink until it meets the inner horizon in annihilation, leaving behind a small shell of strictly positive mass density that expands and disperses. The amount of mass lost during this non-conservative "evaporation" phase seems numerically to be arbitrarily small for horizons forming in the quantum region which evaporate very soon after formation (for $\mu/r_{oh,max} \sim 1$). For larger black holes ($\mu/r_{oh,max} \sim 1/5$) we observed

[6]The ordinate in these animations is rescaled at each frame in order to keep the entire mass density in the plotted range.

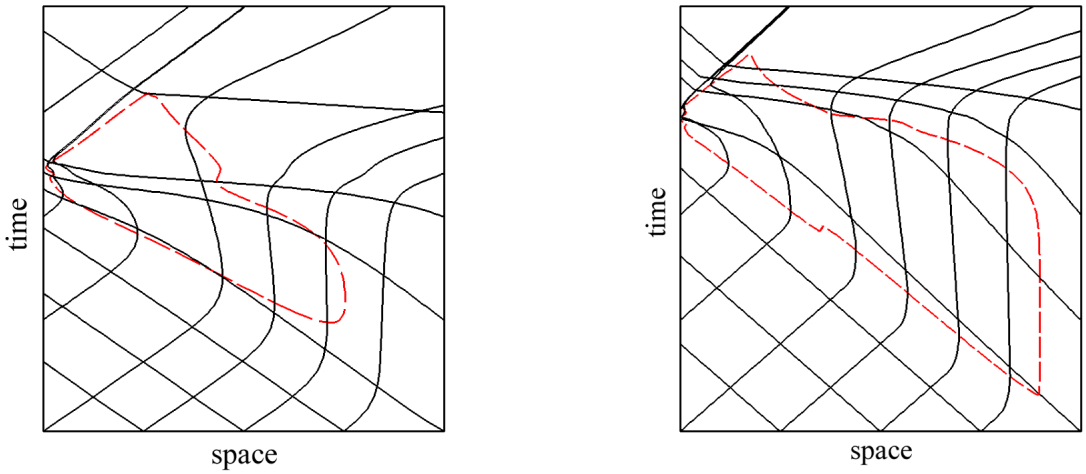

(a) tanh initial data

(b) gaussian initial data

Figure 2.9: Diagrams of the quantum spacetime for the collapsing massless scalar field using radius for the space axis and PG time for the time axis. The solid black lines are null geodesics and the dashed red lines indicate the trapping surface boundary.

mass losses of 80%, and higher values are likely possible. One can speculate that the quantum corrected collapse of macroscopic black holes would also leave microscopic shells with radii of order μ.

According to Einstein's field equations, the energy density measured by an observer at constant r is

$$\rho = \frac{\mathcal{M}'}{4\pi r^2}. \tag{2.6.7}$$

The negative mass density near the quantum bounce thus implies a violation of the null and dominant energy conditions inside the black hole. Such violations are also expected [54] in the presence of Hawking radiation.

For a time after the outer horizon reaches its maximum and before it starts moving inward, the spacetime appears from the exterior to be that of a static black hole. The amount of time that the outer horizon remains stationary depends upon the distance the

mass has to travel from $r = r_{oh}$ down to the quantum region near $r \sim \mu$. The shape of the mass distribution is also a factor since even for $r_{oh} \gg \mu$, the outer horizon may continue to grow until the onset of evaporation if the infalling mass is spread out over a distance of the same magnitude or greater than r_{oh}. By adjusting the initial mass distribution and μ, the lifetime of the seemingly classical black hole can be made arbitrarily large or small. Notice the outer horizon in Fig. 2.9(b) reaches a maximum and stays constant for a much longer time than the outer horizon in Fig. 2.9(a).

In the study by Hayward [55], a small length parameter was used to effectively preclude singularity formation. A Vaidya-like region with positive ingoing energy flux was matched to a stationary black hole spacetime to model black hole formation. After an arbitrary "time" given by the null coordinate v, a Vaidya-like region with negative ingoing energy flux was matched to the stationary black hole to model evaporation. The negative energy flux was balanced by outgoing Hawking radiation in order to conserve energy. This scenario bears a striking similarity to the black hole evolution produced by our numerical simulations, suggesting that the disappearing mass in our system is in some sense being radiated away, despite the fact that we have not included Hawking radiation directly. The key point in our analysis is that the quantum correction contains a repulsive core that prevents the inner horizon from reaching the origin so that the singularity cannot form. The subtle (non-local) interplay between the microscopic behaviour of the potential and the dynamics of the outer horizon, accompanied by violations of the energy conditions, results in acausal behavior of the semiclassical system. Moreover, since some of the mass that went into the black hole is left behind to disperse after "evaporation", our semiclassical scenario has more than one feature relevant to the ultimate resolution of the information loss paradox.

The quantum mass scaling results for a range of μ values are given in Fig. 2.10. The new feature here is a change in the critical parameter (which we refer to as p_{q*}) that is dependant

upon the choice of quantum length scale μ. Note that for very small $\mu \ll \Delta r(0)$, as is the case for $\mu = 10^{-10}$, the system is numerically identical to the classical case. For larger μ (though still small enough to allow for black holes near enough to criticality) the solutions exhibit critical scaling for some range of $p > p_{q*}$ and come to an abrupt stop at $p = p_{q*}$, below which no black holes form. This is the mass gap predicted by quantum gravity [53], and recently found [51] using a numerical model in null coordinates with similar corrections to those used here. It is interesting that in PG coordinates a large p_{q*} does not necessarily correspond to a larger mass for this value of the parameter due to the non-monotonic, large amplitude oscillations.

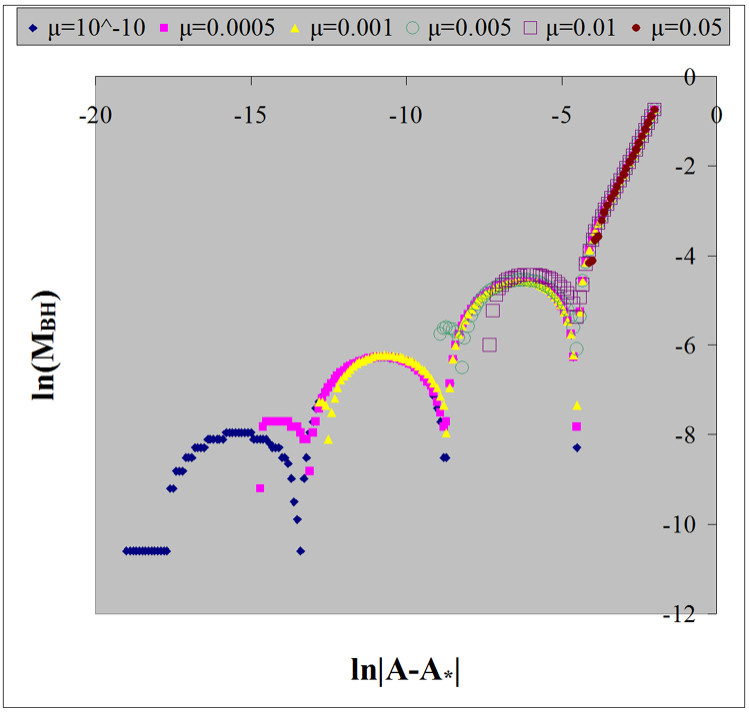

Figure 2.10: A plot of the supercritical mass scaling behaviour with quantum corrections. The parameter A in tanh initial data was varied on a mesh with $\Delta r = 10^{-4}$ near the origin. Each curve corresponds to a different choice of the quantum length scale μ.

Remarkably, we find a quantum power scaling relation near criticality with a universal

exponent:

$$p_{q*} = k_p \left(\frac{\mu}{l}\right)^{\beta} + p_*, \tag{2.6.8}$$

where p_* is the classical critical parameter, k_p is a family dependant constant, l is the length parameter required for proper units and β is a universal constant. This was verified for both forms of initial data with the two choices of the parameter $p = A, B/l$. The results are presented in Fig. 2.11.

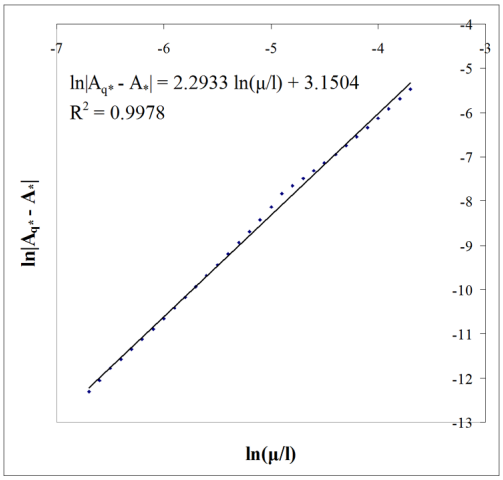

(a) Variation in the parameter A in tanh initial data. The linear fit yields $\beta = 2.29 \pm 0.04$ with 95% confidence.

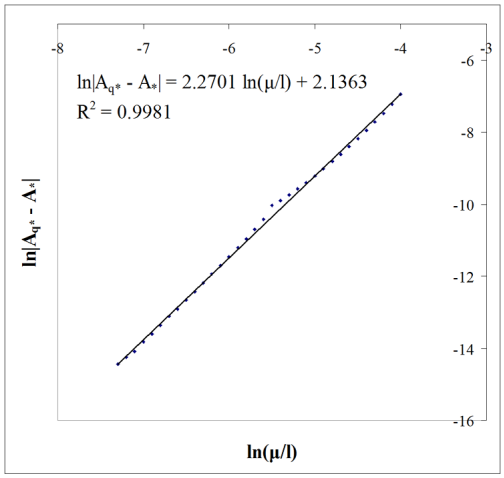

(b) Variation in the parameter A in gaussian initial data. The linear fit yields $\beta = 2.27 \pm 0.03$ with 95% confidence.

Figure 2.11: Each point on these plots is found by setting the quantum length scale μ, then using a binary search to find the critical value of one of the paramters p_{q*}, a rather tedious process. Due to the length of time required to gather this data, the binary search accuracy was reduced to $\partial p/p = 10^{-7}$ for these plots. The regions where the curves deviate from linearity are for parameter ranges causing black hole formation near one of the cusps in the mass scaling behaviour, where the system is very sensitive to small changes in the parameter. While the resolution used here in finding p_{q*} allowed for good linear fits in a reasonable amount of computation time, improving the accuracy of the binary search would likely produce data that follows the line more closely.

2.7 Conclusion

We have derived a set of equations describing the gravitational collapse of a massless scalar field in spherically symmetric coordinates that are regular across apparent horizons. A numerical code was developed to solve these equations providing the means to study black hole formation and evolution in this setting. We showed explicitly that apparent horizons form in pairs with the number of pairs depending on the complexity of initial data. The inner horizon of classical collapse reaches the origin at the onset of singularity formation. LQG suggests that the underlying discreteness at the quantum level will give rise in the semiclassical limit to an effective short range repulsive component to the gravitational potential which in turn can lead to singularity avoidance [57, 58]. Our results agree with this prediction. We incorporated LQG motivated corrections and observed the inner horizon to "bounce" near the quantum length scale, while the outer horizon moves inward due to black hole mass loss. Ultimately, the inner and outer horizons annihilate leaving behind an outward moving spherical shell of mass that disperses to inifinity, a feature that may be relevant to the resolution of the information loss paradox. Although many questions remain, our analysis provides tantalizing support for singularity avoidance in dynamical black hole formation.

In our study of classical Choptuik scaling, we found the (coordinate invariant) curvature scaling to show the same form as in previous studies, while the (coordinate dependant) mass scaling relation revealed an interesting large amplitude component to the oscillations. According to Gundlach [40] the function f that determines the oscillations is universal. However, the location and time of formation of the initial apparent horizon can depend on the choice of spacetime slicing. Ours is the first calculation in PG coordinates. These are non-static coordinates for which data are specified on spacelike surfaces that are regular across future horizons. These unique features of PG coordinates are undoubtedly at the root

of the new periodic form in the mass scaling relationship. It is therefore of great interest to continue the near critical evolution past initial horizon formation in order to study explicitly the scaling relation of the final horizon radius (i.e. the *event* horizon), which should be independent of spacetime slicing. Our attempts to do this have so far failed because near criticality in PG coordinates the singularity forms before the outer horizon settles down to its final value. In this regard it should be noted that PG coordinates constitute a special representative of a one-parameter family of similar coordinates found initially by Lake [59] and developed further in [60]. It may be that by adjusting the parameter one can arrange for the horizon to settle down before singularity formation near criticality. As well, it is important to check whether the cusp-like behaviour is generic for such a family of slicings.

We investigated the affects of quantum corrections on critical scaling. Along any one-parameter family of initial data, a new critical paramter p_{q*} was found that placed a limit on the minimum size of black holes that could be formed. This mass gap is expected and was also found recently by Husain [51] using similar quantum corrections in double null coordinates. Curiously, we find a new universal power law relationship between p_{q*} and the quantum length scale. Recall that the radial coordinate is common between the Schwarzschild and PG metrics. It would therefore be worthwhile to apply similar corrections to a model which uses Schwarzschild coordinates, and investigate the universality of this new scaling law.

Epilogue

In this thesis we have studied a particle in the $1/r^2$ potential and a massless scalar field coupled to a spherically symmetric gravitational potential. In both cases LQG motivated corrections were shown to preclude singularity formation, and computational methods proved to be integral in the process.

The iterative shooting method used to apply full polymerization to the $1/r^2$ potential worked very naturally with the discrete position eigenstates. We found an inner turning point preventing a particle from reaching the origin in a $1/r^2$ potential. It would be interesting to apply the same quantization techniques to theories more closely related to LQG.

The study of gravitational collapse involved a more complicated computer code, requiring adaptive mesh refinement, Runge-Kutta numerical integration and finite difference methods; there were many fields to be solved for across the entire lattice, and producing the results was more involved. In the end this effort payed off, clearly demonstrating previously unseen behaviour in both the classical and quantum systems. Unlike any previous study we are aware of, we were able to solve for the entire (interior and exterior) dynamical black hole solution. With the quantum corrections in place, the scalar field inside a black hole experiences a dramatic bounce near the origin, precluding the existence of singularities and leading ultimately to evaporation. There is much more that can be done with this model. Since we use the dilaton formalism, it would be possible to take the number of dimensions

as a parameter and compare the results with the dimensional analyses done in [45] and [61]. We are currently looking at the subcritical curvature scaling relationship in the presence of quantum corrections. Since we have altered the equations of motion, the field equations are no longer valid in the quantum case, and the Ricci calculations must be done using the metric functions, dramatically increasing the time of computation. We plan to look further into the energy condition violations. LQG theory has predicted violations of the null energy condition when the scalar field behaves after the bounce as a phantom field with negative mass energy [53]. We have already seen some evidence of this in the negative energy density and mass loss in quantum collapse.

Bibliography

[1] G. Amelino-Camelia, "Quantum Gravity Phenomenology", arXiv:0806.0339v1 [gr-qc] (2008).

[2] A. Ashtekar, T. Pawlowski and P. Singh, "Quantum nature of the big bang: Improved dynamics", Phys. Rev. D **74**, 084003 (2006) [arXiv:gr-qc/0607039]; A. Ashtekar, T. Pawlowski, P. Singh and K. Vandersloot, "Loop quantum cosmology of k = 1 FRW models", Phys. Rev. D **75**, 024035 (2007) [arXiv:gr-qc/0612104]; K. Vandersloot, "Loop quantum cosmology and the $k = -1$ RW model", Phys. Rev. D **75**, 023523 (2007) [arXiv:gr-qc/0612070].

[3] M. Martin-Benito, L. J. Garay and G. A. Mena Marugan, "Hybrid Quantum Gowdy Cosmology: Combining Loop and Fock Quantizations", Phys. Rev. D **78**, 083516 (2008).

[4] V. Husain and O. Winkler, "Quantum Hamiltonian for gravitational collapse", Phys. Rev. D **73**, 124007 (2006) [arXiv:gr-qc/0601082].

[5] A. Ashtekar and M. Bojowald, "Quantum geometry and the Schwarzschild singularity", Class. Quant. Grav. **23**, 391 (2006) [arXiv:gr-qc/0509075].

[6] L. Modesto, "Black hole interior from loop quantum gravity", arXiv:gr-qc/0611043; C. G. Boehmer and K. Vandersloot, "Loop Quantum Dynamics of the Schwarzschild Interior", Phys. Rev. D **76**, 104030 (2007) [arXiv:0709.2129 [gr-qc]]; "Stability of the Schwarzschild Interior in Loop Quantum Gravity", arXiv:0807.3042 [gr-qc]; M. Campiglia, R. Gambini and J. Pullin, "Loop quantization of spherically symmetric midi-superspaces : the interior problem", AIP Conf. Proc. **977**, 52 (2008) [arXiv:0712.0817 [gr-qc]]; R. Gambini and J. Pullin, "Black holes in loop quantum gravity: the complete space-time", Phys. Rev. Lett. **101**, 161301 (2008) [arXiv:0805.1187 [gr-qc]].

[7] A. Ashtekar, "Polymer Geometry at Planck Scale and Quantum Einstein Equations", Int. J. Mod. Phys. D **5**, 629 (1996).

[8] P. Painlevé, "La mécanique classique et la théorie de la relativité", C. R. Acad. Sci. (Paris) **173** 677 (1921).

[9] A. Gullstrand, "Allgemeine Lösung des statischen Einkrperproblems in der Einsteinschen Gravitationstheorie", Arkiv. Mat. Astron. Fys. **16**(8) 1 (1922).

[10] T. Thiemann, *Modern Canonical Quantum General Relativity*, Cambridge University Press, Cambridge (2007).

[11] T. Thiemann, "Quantum spin dynamics (QSD)", Class. Quant. Grav. **15**, 839 (1998) [arXiv:gr-qc/9606089].

[12] A. Ashtekar, S. Fairhurst and J. L. Willis, "Quantum gravity, shadow states, and quantum mechanics", Class. Quant. Grav. **20**, 1031 (2003) [arXiv:gr-qc/0207106].

[13] H. Halvorson, "Complementarity of representations in quantum mechanics", Studies Hist. Philos. Mod. Phys. **35**, 45 (2004) [arXiv:quant-ph/0110102].

[14] C. J. Fewster, "On the energy levels of the hydrogen atom", arXiv:hep-th/9305102.

[15] J. Louko and J. Mäkelä, "Area spectrum of the Schwarzschild black hole", Phys. Rev. D **54**, 4982 (1996) [arXiv:gr-qc/9605058].

[16] V. Husain, J. Louko and O. Winkler, "Quantum gravity and the Coulomb potential", Phys. Rev. D **76**, 084002 (2007) [arXiv:0707.0273 [gr-qc]].

[17] L. Motl, "An analytical computation of asymptotic Schwarzschild quasinormal frequencies", Adv. Theor. Math. Phys. **6**, 1135 (2003) [arXiv:gr-qc/0212096].

[18] G. Kunstatter, "d-dimensional black hole entropy spectrum from quasi-normal modes", Phys. Rev. Lett. **90**, 161301 (2003) [arXiv:gr-qc/0212014].

[19] H. E. Camblong and C. R. Ordonez, "Black hole thermodynamics from near-horizon conformal quantum mechanics", Phys. Rev. D **71**, 104029 (2005) [arXiv:hep-th/0411008].

[20] J. Gegenberg, G. Kunstatter and R. D. Small, "Quantum structure of space near a black hole horizon", Class. Quant. Grav. **23**, 6087 (2006) [arXiv:gr-qc/0606002].

[21] K. M. Case, "Singular Potentials", Phys. Rev. **80**, 797 (1950).

[22] W. M. Frank, D. J. Land and R. M. Spector, "Singular Potentials", Rev. Mod. Phys. **43**, 36 (1971).

[23] H. Narnhofer, "Quantum theory for $1/r^2$-potentials", Acta Phys. Austriaca **40**, 306 (1974).

[24] K. S. Gupta and S. G. Rajeev, "Renormalization in quantum mechanics", Phys. Rev. D **48**, 5940 (1993) [arXiv:hep-th/9305052].

[25] H. E. Camblong, L. N. Epele, H. Fanchiotti and C. A. Garcia Canal, "Renormalization of the inverse square potential", Phys. Rev. Lett. **85**, 1590 (2000) [arXiv:hep-th/0003014]; "Dimensional transmutation and dimensional regularization in quantum mechanics. I: General theory", Annals Phys. **287**, 14 (2001) [arXiv:hep-th/0003255].

[26] H. E. Camblong and C. R. Ordonez, "Renormalization in conformal quantum mechanics", Phys. Lett. A **345**, 22 (2005) [arXiv:hep-th/0305035]; "Anomaly in conformal quantum mechanics: From molecular physics to black holes", Phys. Rev. D **68**, 125013 (2003) [arXiv:hep-th/0303166]; G. N. J. Ananos, H. E. Camblong and C. R. Ordonez, "SO(2,1) conformal anomaly: Beyond contact interactions", Phys. Rev. D **68**, 025006 (2003) [arXiv:hep-th/0302197].

[27] H. E. Camblong, L. N. Epele, H. Fanchiotti, C. A. Garcia Canal and C. R. Ordonez, "On the Inequivalence of Renormalization and Self-Adjoint Extensions for Quantum Singular Interactions", Phys. Lett. A **364**, 458 (2007) [arXiv:hep-th/0604018].

[28] T. Fúlöp, *Symmetry, Integrability and Geometry, Proceedings of the 3rd Microconference "Analytic and Algebraic Methods III"*, http://www.emis.de/journals/SIGMA/Prague2007.html

[29] W. E. Thirring, *Quantum mathematical physics*, 2nd edition (Springer, Berlin, 2002).

[30] *Handbook of Mathematical Functions*, edited by M. Abramowitz and I. A. Stegun (Dover, New York, 1965).

[31] A. Corichi, T. Vukasinac and J. A. Zapata, "Polymer Quantum Mechanics and its Continuum Limit", Phys. Rev. D **76**, 044016 (2007) [arXiv:0704.0007 [gr-qc]].

[32] N. Andersson and C. J. Howls, "The asymptotic quasinormal mode spectrum of non-rotating black holes", Class. Quant. Grav. **21**, 1623 (2004) [arXiv:gr-qc/0307020].

[33] I. S. Gradshteyn and I. M. Ryzhik, *Table of Integrals, Series and Products*, 4th edition (Academic, New York, 1980).

[34] M. Reed and B. Simon, *Methods of Modern Mathematical Physics II: Fourier Analysis, Self-adjointness* (Academic, New York, 1975).

[35] S. Elaydi, *An Introduction to Difference Equations*, 3rd edition (Springer, New York, 2005).

[36] A. Ashtekar, A. Corichi and P. Singh, "On the robustness of key features of loop quantum cosmology", Phys. Rev. D **77**, 024046 (2008) [arXiv:0710.3565 [gr-qc]].

[37] A. Corichi and P. Singh, "Is loop quantization in cosmology unique?", Phys. Rev. D **78**, 024034 (2008) [arXiv:0805.0136 [gr-qc]].

[38] W. Kaminski and J. Lewandowski, "The flat FRW model in LQC: the self-adjointness", Class. Quant. Grav. **25**, 035001 (2008) [arXiv:0709.3120 [gr-qc]].

[39] M.W. Choptuik, "Universality and Scaling in Gravitational Collapse of a Massless Scalar Field", Phys. Rev. Lett. **70**(1) 9 (1993).

[40] C. Gundlach, "Understanding critical collapse of a scalar field", Phys. Rev. D **55**(2) 695 (1997).

[41] S. Hod and T. Piran, "Fine structure of Choptuik's mass-scaling relation", Phys. Rev. D **55**(2), 440 (1997).

[42] D. Garfinkle, G. Duncan, "Scaling of curvature in sub-critical gravitational collapse", Phys. Rev. D **58** 064024 (1998).

[43] D. Garfinkle, "Choptuik Scaling in Null Coordinates", Phys. Rev. D **51**, 5558 (1995).

[44] R.S. Hamade and J. M. Stewart, "The spherically symmetric collapse of a massless scalar field", Class. Quantum Grav. **13**, 497 (1996).

[45] J. Bland, G. Kunstatter, M. Becker and B. Preston and V. Husain, "Dimension-Dependence of the Critical Exponent in Spherically Symmetric Gravitational Collapse", Class. Quantum Grav. **22** 5355 (2005).

[46] D. Grumiller, W. Kummer and D.V. Vassilevich, "Dilaton gravity in two dimensions", Phys. Rept. **369** 327 (2002).

[47] G. Kunstatter, R. Petryk and S. Shelemy, "Hamiltonian Thermodynamics of Black Holes in Generic 2-D Dilaton Gravity", Phys. Rev. D **57**, 3537 (1998).

[48] R. Arnowitt, S. Deser, C.W. Misner, "The Dynamics of General Relativity", 1962, in *Gravitation: an Introduction to Current Research* by L. Witten, ch. 7, pp. 227-265.

[49] R.G. Daghigh, J. Gegenberg and G. Kunstatter, "A Partially Gauge Fixed Hamiltonian for Scalar Field Collapse", Class. Quant. Grav. **24** 2099 (2007).

[50] For a comparison with PG coordinates using a dilaton formalism in the case of a vacuum, see G. Kunstatter and J. Louko, "Transgressing the horizons: time operator in two dimensional dilaton gravity", Phys. Rev. D **75** 024036 (2007).

[51] V. Husain, "Critical behaviour in quantum gravitational collapse", arXiv: 0808.0949v1 [gr-qc] (2008).

[52] For a recent discussion of trapping surfaces see S. Hayward, "Dynamics of black holes", arXiv:0810.0923v1 [gc-qc] (2008).

[53] M. Bojowald, R. Goswami, R. Maartens, P. Singh, "A black hole mass threshold from non-singular quantum gravitational collapse", Phys. Rev. Lett. **95**, 091302 (2005).

[54] M. Visser, " Gravitational vacuum polarization I: Energy conditions in the Hartle–Hawking vacuum", Phys. Rev. D **54**, 5103 (1996).

[55] S. Hayward, "Formation and evaporation of non-singular black holes", Phys. Rev. Lett. 96 031103 (2006).

[56] J. Bland, *Dimension Dependence of the Critical Phenomena in Gravitational Collapse of Massless Scalar Field*, Ph.D. thesis, University of Manitoba (2007).

[57] A. Ashtekar and M. Bojowald, "Quantum Geometry and the Schwarzschild Singularity", Class. Quant. Grav. **23**, 391 (2006) [arXiv:gr-qc/0509075].

[58] L. Modesto, "Loop Quantum Black Hole", Class. Quant. Grav. **23**, 5587 (2006) [arXiv:gr-qc/0509078]; "Black Hole Interior from Loop Quantum Gravity", arXiv:gr-qc/0611043; C. G. Boehmer and K. Vandersloot, "Loop Quantum Dynamics of the Schwarzschild Interior", Phys. Rev. D **76**, 104030 (2007) [arXiv:0709.2129 [gr-qc]]; M. Campiglia, R. Gambini and J. Pullin, "Loop Quantization of Spherically Symmetric Midi-Superspaces : The Interior Problem", AIP Conf. Proc. **977**, 52 (2008) [arXiv:0712.0817 [gr-qc]]; R. Gambini and J. Pullin, "Black holes in Loop Quantum Gravity: the Complete Space-Time", arXiv:0805.1187 [gr-qc].

[59] K. Lake, "A Class of quasi-stationary regular line elements for the Schwarzschild geometry", [gr-qc/9407005] (1994).

[60] K. Martel and E. Poisson, "Regular coordinate systems for Schwarzschild and other spherical spacetimes", Am. J. Phys. **69**, 476 (2001).

[61] D. Garfinkle, C. Cutler and G. Duncan, "Choptuik scaling in six dimensions", Phys.Rev. D **60** 104007 (1999).